Supplementary Information

Corrosion-resistant and high-entropic non-noble metal bifunctional electrodes for PEM-type water electrolyser

Supplementary methods

Surface area measurement. The surface areas of the samples were measured by the Brunauer-Emmett-Teller (BET) method using a BELSORP-MAX (BEL. JAPAN. INC) at −196 °C. The horizontal axis was normalized with the vapor pressure of nitrogen (P_0) at −196 °C (=0.101 MPa). The samples were heated at 120 °C under vacuum for 24 h before the measurements.

Evaluation of energy diagram by density functional theory. For the hydrogen evolution reaction (HER), the hydrogen adsorption energy (ΔE_{H*}) was calculated as:

$$\Delta E_{H*} = \frac{1}{n}(E_{tot} - E_{sub}) - \frac{1}{2}E_{H_2}, \quad (1)$$

where E_{tot} was the total energy of the substrate with n hydrogen atoms adsorbed on the surface, E_{sub} was the total energy of the substrate, and E_{H_2} was the energy of a hydrogen molecule in the gas phase (about -6.7eV was employed in this work). The Gibbs free energy for the hydrogen absorption was corrected as:

$$\Delta G_H = \Delta E_{H*} + \Delta E_{ZPE} - T\Delta S_H, \quad (2)$$

where ΔE_{ZPE} was the difference in zero point energy between the adsorbed hydrogen and hydrogen in the gas phase and ΔS_H was the entropy difference between the adsorbed state and the gas phase. As the contribution from the vibrational entropy of H* in the adsorbed state was negligibly small, the entropy of hydrogen adsorption was $\Delta S_{H*} \approx -\frac{1}{2}S_{H_2}$, where S_{H_2} was the entropy of H_2 in the gas phase. Then the Gibbs free energy with the overall corrections can be calculated as $\Delta G_{H*} = \Delta E_{H*} + 0.24$ eV. We computed ΔG_{H*} for 1796 sites.

For the oxygen evolution reaction (OER), we considered the four elementary steps:

$$H_2O_{(l)} + * \rightarrow OH* + H^+/e^- \quad (3)$$

$$OH* \rightarrow O* + H^+/e^- \quad (4)$$

$$O* + H_2O_{(l)} \rightarrow OOH* + H^+/e^- \quad (5)$$

$$OOH* \rightarrow O_2(g) + * + H^+/e^- \quad (6)$$

where * represented a surface site and OH*, O*, and OOH* were intermediates adsorbed on an active site on the catalyst surface. The free energy of each intermediate was calculated at 0 V vs standard hydrogen electrode (SHE) by referencing liquid water and hydrogen gas at standard conditions:

$$\Delta G_{\mathrm{OH}*} = E_{\mathrm{OH}*}^{\mathrm{DFT}} - E_{*}^{\mathrm{DFT}} - E_{\mathrm{H_2O}}^{\mathrm{DFT}} + \frac{1}{2}E_{\mathrm{H_2}}^{\mathrm{DFT}} + \hat{G}_{\mathrm{OH}} \quad (7)$$

$$\Delta G_{\mathrm{O}*} = E_{\mathrm{O}*}^{\mathrm{DFT}} - E_{*}^{\mathrm{DFT}} - E_{\mathrm{H_2O}}^{\mathrm{DFT}} + E_{\mathrm{H_2}}^{\mathrm{DFT}} + \hat{G}_{\mathrm{O}} \quad (8)$$

$$\Delta G_{\mathrm{OOH}*} = E_{\mathrm{OOH}*}^{\mathrm{DFT}} - E_{*}^{\mathrm{DFT}} - 2E_{\mathrm{H_2O}}^{\mathrm{DFT}} + \frac{3}{2}E_{\mathrm{H_2}}^{\mathrm{DFT}} + \hat{G}_{\mathrm{OH}} \quad (9)$$

where E_{*}^{DFT}, $E_{\mathrm{OH}*}^{\mathrm{DFT}}$, $E_{\mathrm{O}*}^{\mathrm{DFT}}$, and $E_{\mathrm{OOH}*}^{\mathrm{DFT}}$ were the ground state energy of the surface and the surface with OH*, O*, and OOH* intermediates, respectively. $E_{\mathrm{H_2O}}^{\mathrm{DFT}}$ and $E_{\mathrm{H_2}}^{\mathrm{DFT}}$ were the energies of H_2O and H_2 molecules, respectively, in the gas phase. $\hat{G}$ included contributions from vibration energy and entropy of the intermediate at 300 K. We employed typical values of 0.35 eV, 0.05 eV, and 0.40 eV for OH*, O*, and OOH*, respectively.[1,2] The standard free energy change of each elementary step can be calculated:

$$\Delta G_1^{\mathrm{o}} = \Delta G_{\mathrm{OH}*} \quad (10)$$

$$\Delta G_2^{\mathrm{o}} = \Delta G_{\mathrm{O}*} - \Delta G_{\mathrm{OH}*} \quad (11)$$

$$\Delta G_3^{\mathrm{o}} = \Delta G_{\mathrm{OOH}*} - \Delta G_{\mathrm{O}*} \quad (12)$$

$$\Delta G_4^{\mathrm{o}} = \Delta G_{\mathrm{O_2(g)}}^{\mathrm{o}} - \Delta G_{\mathrm{OOH}*} \quad (13)$$

$$\Delta G_{\mathrm{O_2(g)}}^{\mathrm{o}} = 4.92\ \mathrm{eV} \quad (14)$$

The theoretical overpotential is given by:

$$\eta = \max\{\Delta G_1^{\mathrm{o}}, \Delta G_2^{\mathrm{o}}, \Delta G_3^{\mathrm{o}}, \Delta G_4^{\mathrm{o}}\} - 1.23 \quad (15)$$

For HER, we added one H atom on top of the surface atoms defined as $|z| > 4.3$ Å, where the center of mass of the slab was set to z=0 and the x and y are surface parallel directions. To evaluate the energy diagram of OER, we firstly added OOH on top of the surface atoms defined as $|z| > 5.4$ Å. The OOH species were decomposed into O and OH

on most of the surface sites, because $\Delta G_{\mathrm{O}*}$ and $\Delta G_{\mathrm{OH}*}$ were generally large for non-noble metals. When the OOH* intermediate survived, we computed $\Delta G_{\mathrm{O}*}$ by removing the O and H atoms from OOH*, and then computed $\Delta G_{\mathrm{OH}*}$ by adding H on O* to complete the energy diagram. We tried 2677 sites for the OOH* adsorption and completed energy diagram for 270 sites, where the OOH* intermediate survived. OER energy diagram was further investigated by oxidized surfaces. We added O atoms on all the surface atoms of one surface model and then computed the energy diagram of OER. $\Delta G_{\mathrm{O}*}$ was significantly reduced because the site was already oxidized, enhancing the OER activity.

Supplementary discussions

Machine learning force field. Development of machine learning force fields (MLFF) has been a rapidly growing research field[3] in recent years. MLFF is a classical force field consisting of highly flexible functions, which are designed to fit any complex data and are not based on physical pictures. The parameters of MLFF are obtained by fitting a large amount of first-principles results. Because of the flexibility of MLFF, it can describe, for example, structures before and after a phase transition[4], which is highly difficult for conventional classical force fields that are designed to describe specific chemical bonds. Although MLFF has begun to be applied to various materials, construction of MLFF for materials containing a large number of atoms (more than four) is highly challenging.

In this work, we employed the Gaussian approximation potential (GAP)[5] model, which is one of the kernel regression type MLFF. First, we constructed GAP potential using 300 snapshots of structure, energy and atomic forces from 30 ps density functional theory molecular dynamics (DFT-MD) trajectory at 3000 K. We included two-body, three-body and smooth overlap of atomic potentials (SOAP)[6] kernels and their cutoff radii were set to 5 Å. When we compared GAP and DFT, the root mean square errors (RMSEs) of the energies and forces are 5 meV/atom and 0.4 eV/Å, respectively. This force RMSE is a bit larger than the typical criterion, 0.1 eV/Å, reflecting the difficulty of generating MLFF for alloys containing as many as nine elements. Nevertheless, the radial distribution function obtained from the MLFF-MD simulations well reproduced that of DFT-MD (Figure S24), which motivated us to employ the GAP potential to accelerate the high temperature MD to efficiently sampling the configurations of 9eHEA.

After collecting snapshots from 5 ps trajectories before optimizing the bulk 9eHEA structures, we again constructed the GAP potential using 600 snapshots. This potential shows a smaller force RMSE of 0.3 eV/Å. In future work, we will extend the GAP potential to describe not only bulk but 9eHEA surfaces without using DFT calculations.

Electronic structure of bulk 9eHEA. Figure S25 shows a bulk 9eHEA structure and its projected density of states (PDOS). 9eHEA is a spin-unpolarized metal and Fe, Mn, Co, Cr contributed to the density of states at the Fermi level as twice as other atoms.

Supplementary Figures

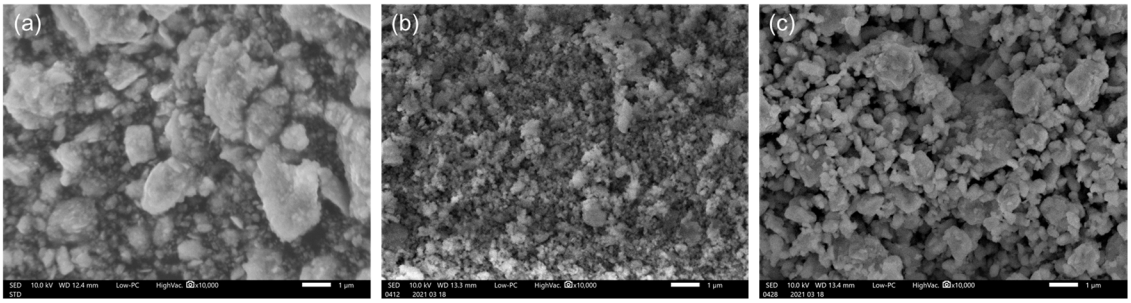

Supplementary Figure 1. SEM images of (a) 4eHEA, (b) 5eHEA and (c) 9eHEA powders after 6 days ball milling.

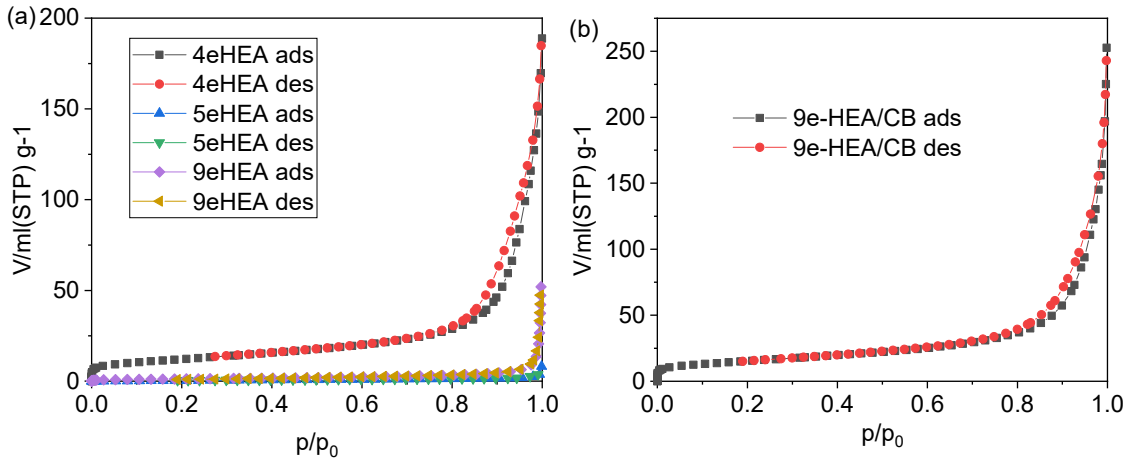

	4eHEA	5eHEA	9eHEA	9eHEA/CB
BET surface area (m^2/g)	43.14	2.70	4.71	55.1

Supplementary Figure 2. Nitrogen adsorption and desorption measurements. The isotherm of (a) 4eHEA, 5eHEA and 9eHEA and (b) 9eHEA/CB with their BET surface area. The large BET surface of 4eHEA could be attributed to the easy-to-crush characteristics.

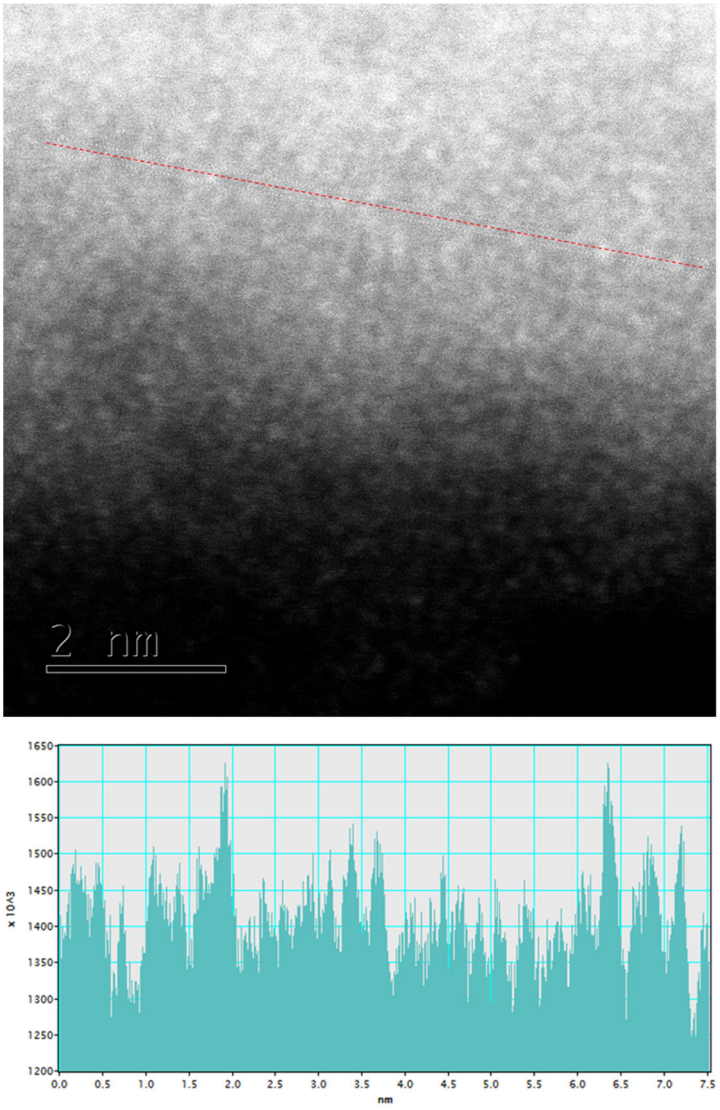

Supplementary Figure 3. Intensity profiles of DF-STEM image in Figure 1d. A Red line showed the position of intensity profile.

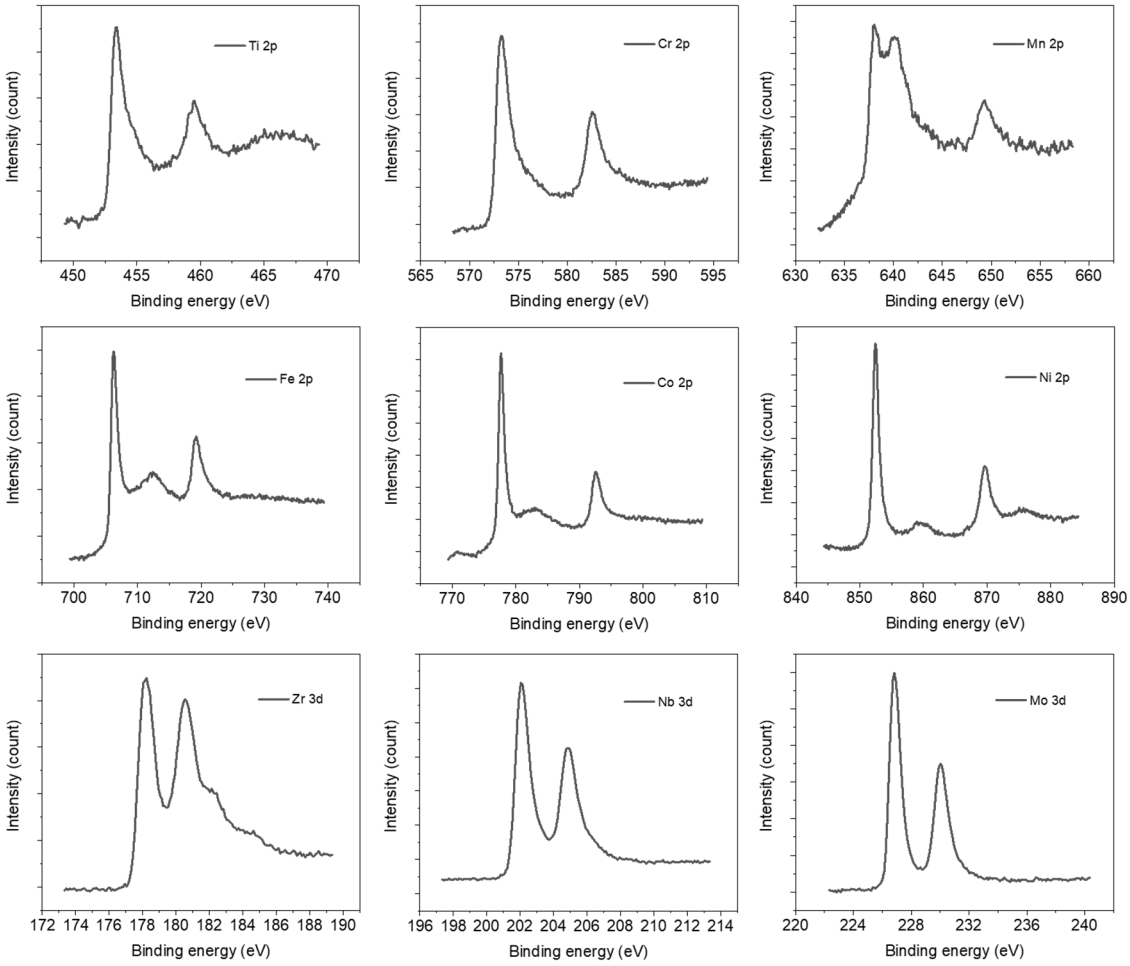

Supplementary Figure 4. XPS spectra of 9eHEA.

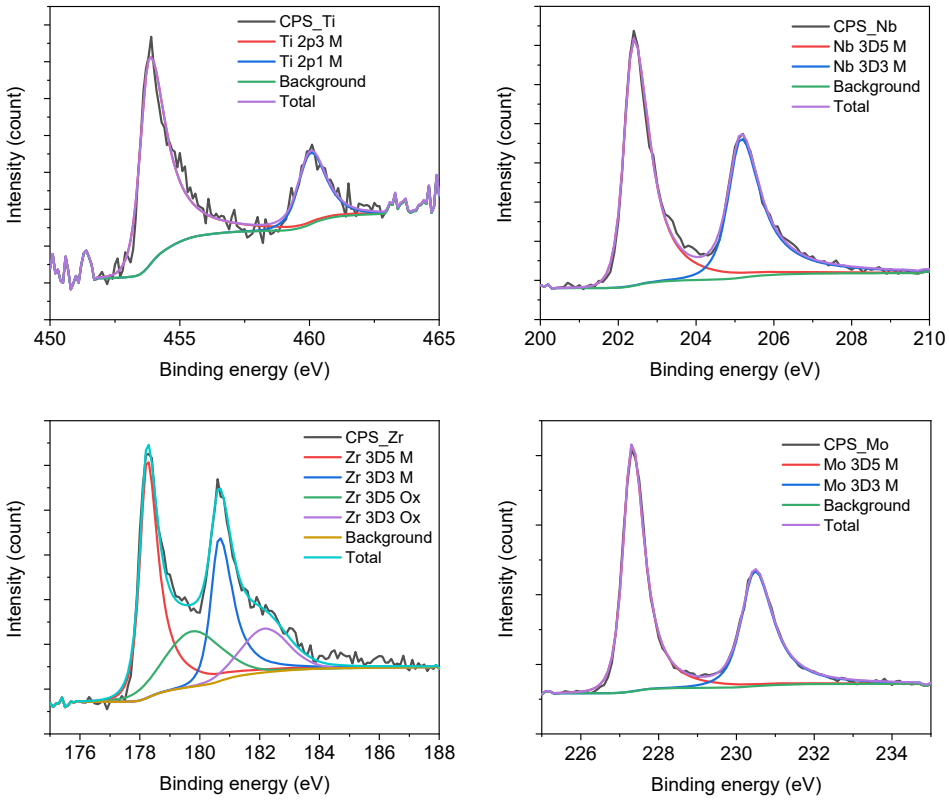

Supplementary Figure 5. XPS spectra of 4eHEA.

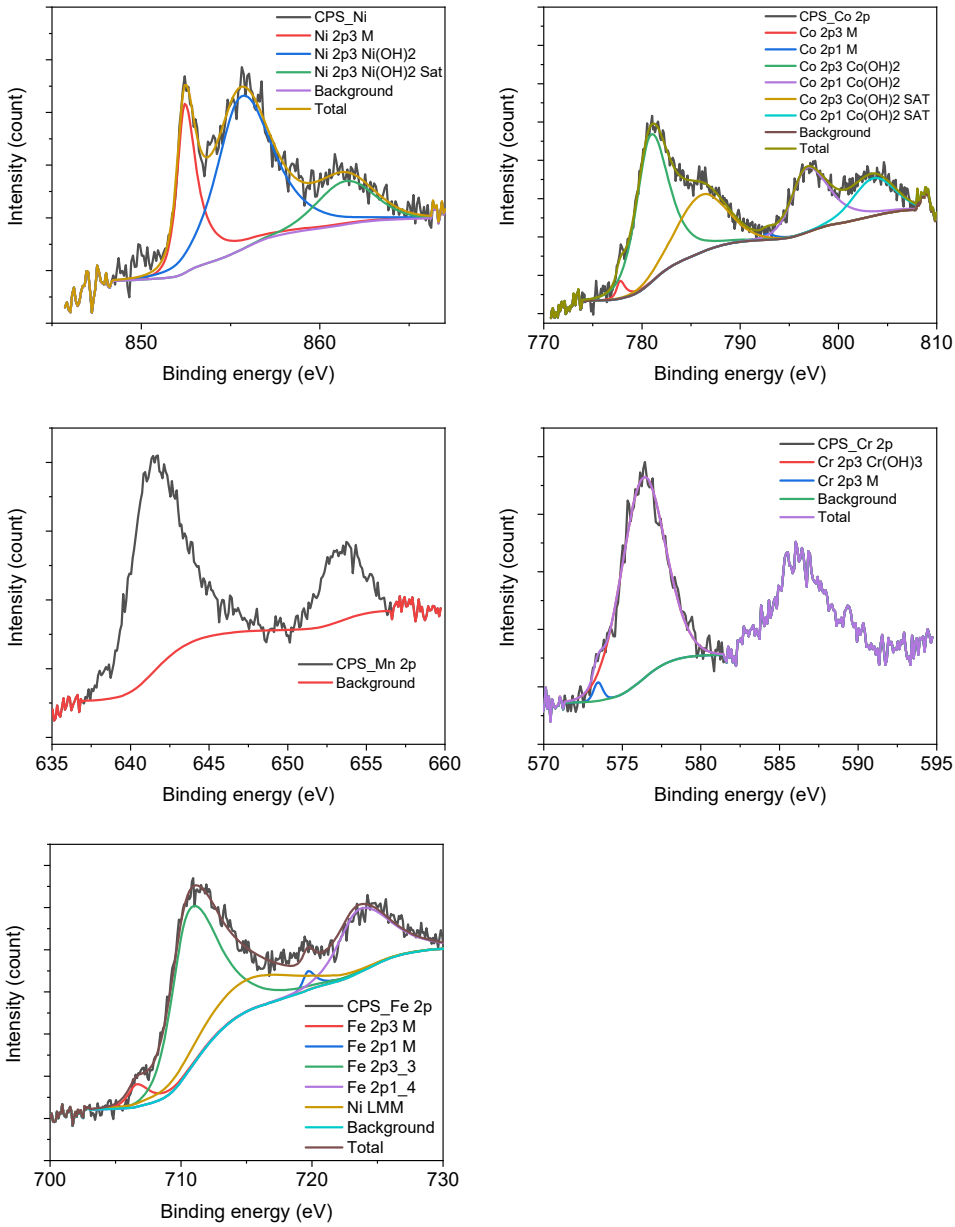

Supplementary Figure 6. XPS spectra of 5eHEA.

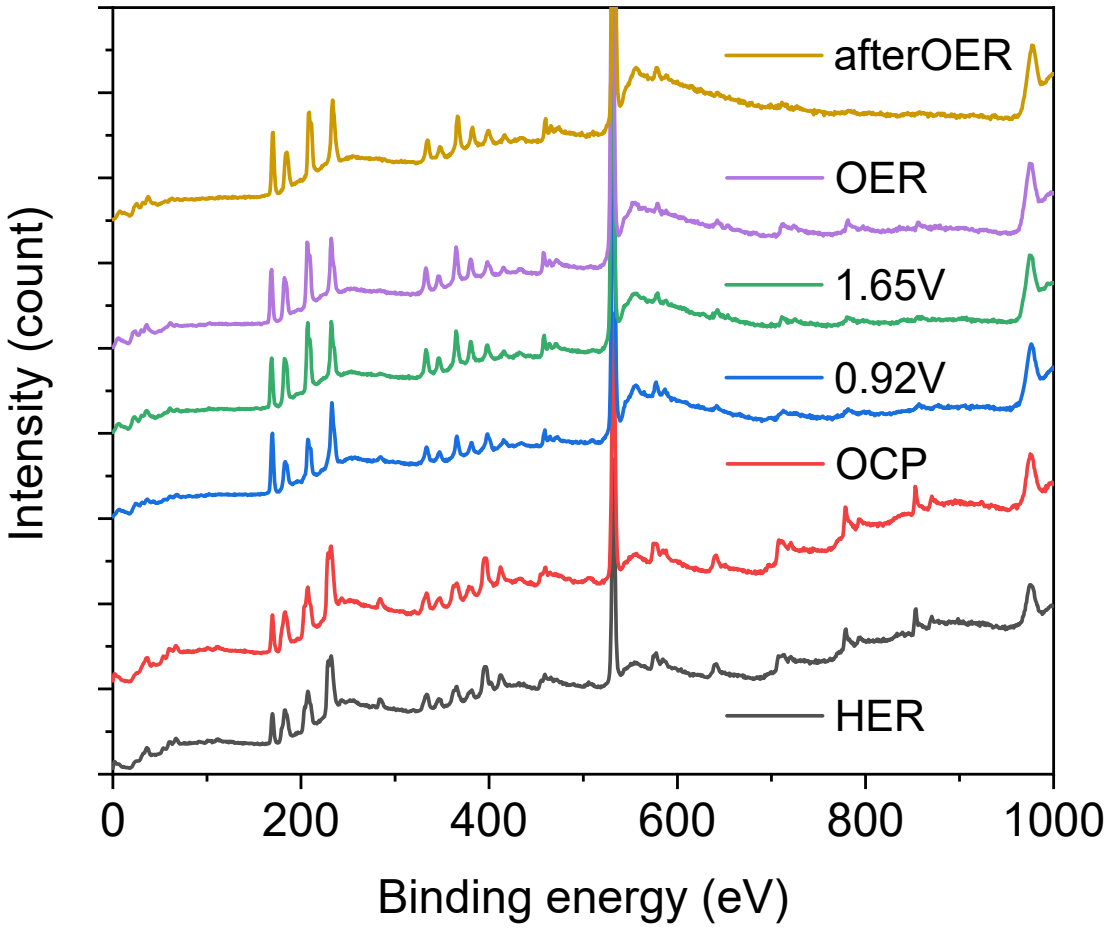

Supplementary Figure 7. Overall EC-XPS at OCP (0.14 V), 1st stage (0.92 V), 2nd stage (1.65 V), OER (1.90 V), after OER (0.07 V) and HER (−0.30 V) at survey mode.

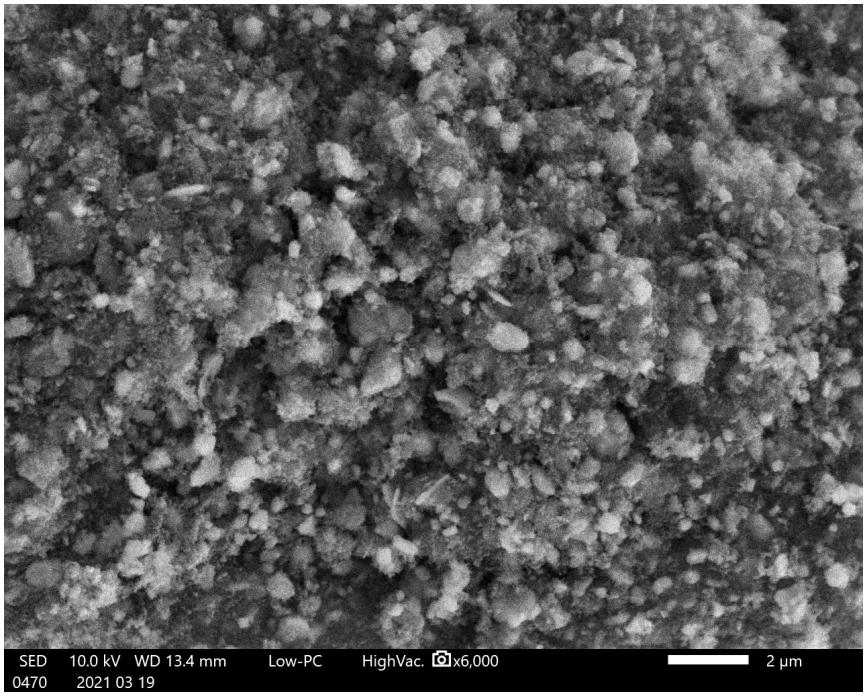

Supplementary Figure 8. A typical SEM image of 9eHEA powders mixed with carbon black before tests.

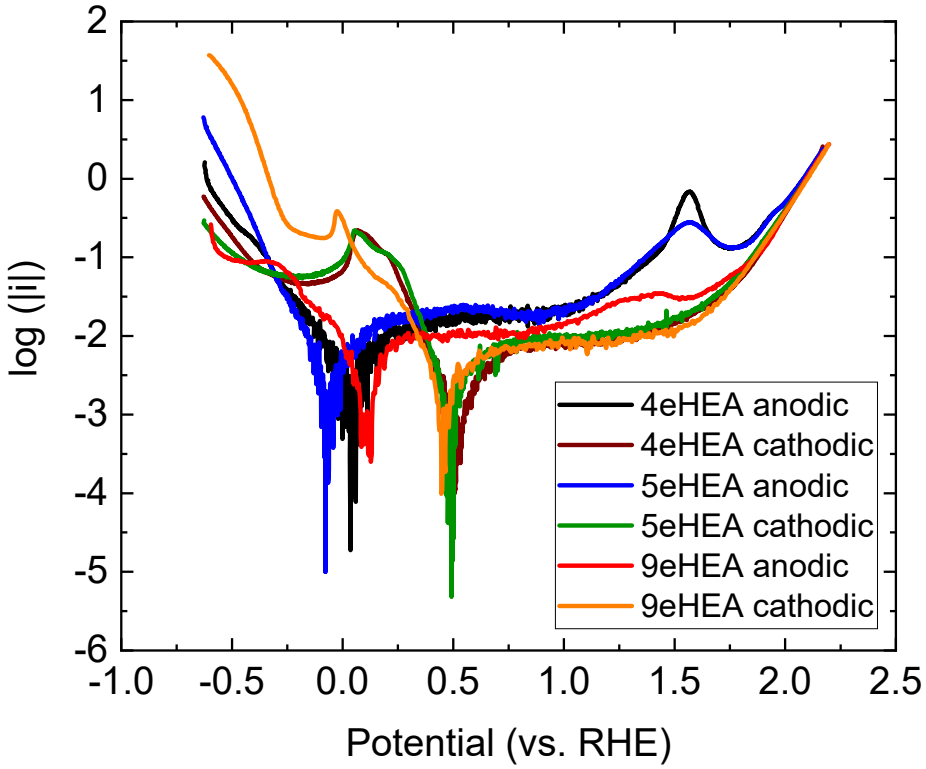

Supplementary Figure 9. Typical corrosion curves with anodic and catholic scans with 0.1 mV/s scan rate in 0.5 M H_2SO_4 electrolyte.

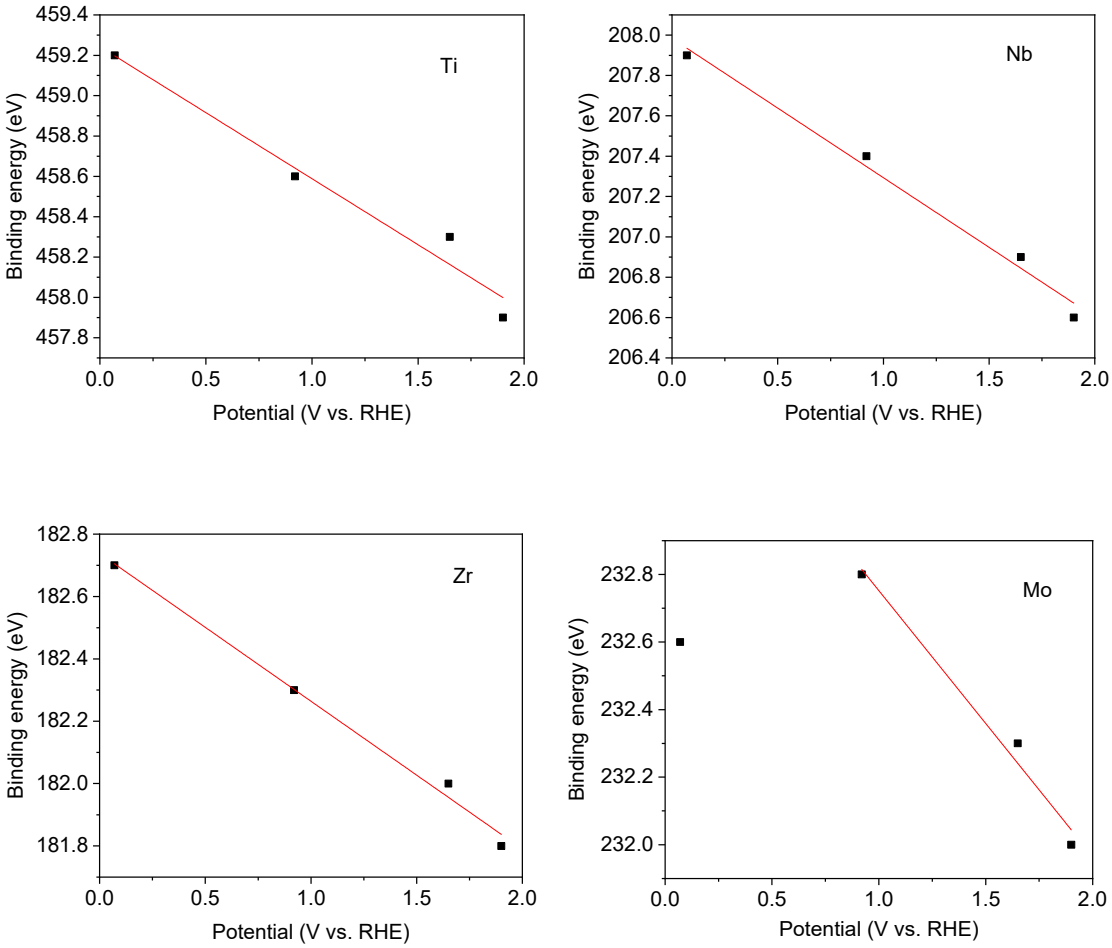

Supplementary Figure 10. Binding energy shift toward the applied potentials. MoO_3 at 1.90 V (vs. RHE) was not reduced to MoO_2 at 0.07 V (vs. RHE) after the OER (1.90 V (vs. RHE)).

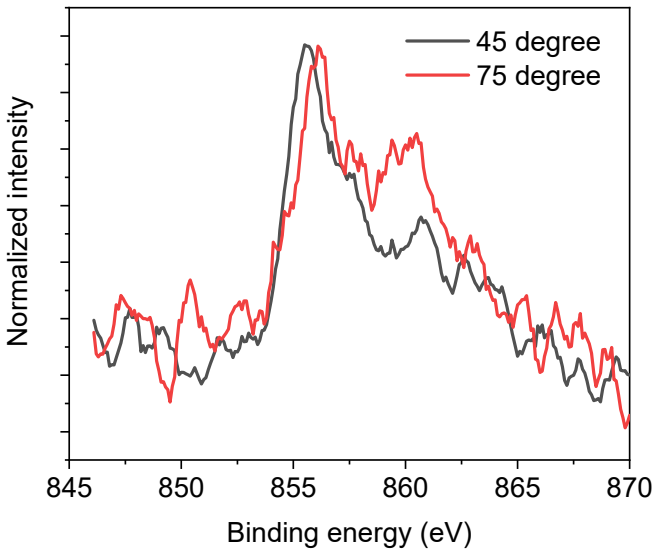

Supplementary Figure 11. Typical angle resolved XPS spectra at 45° and 75° for Ni. Quantitative estimation of Fe, Ni, Co in our analysis included the shake-up satellite peak (but excluded their Auger peaks) due to the empty of d band.[7]

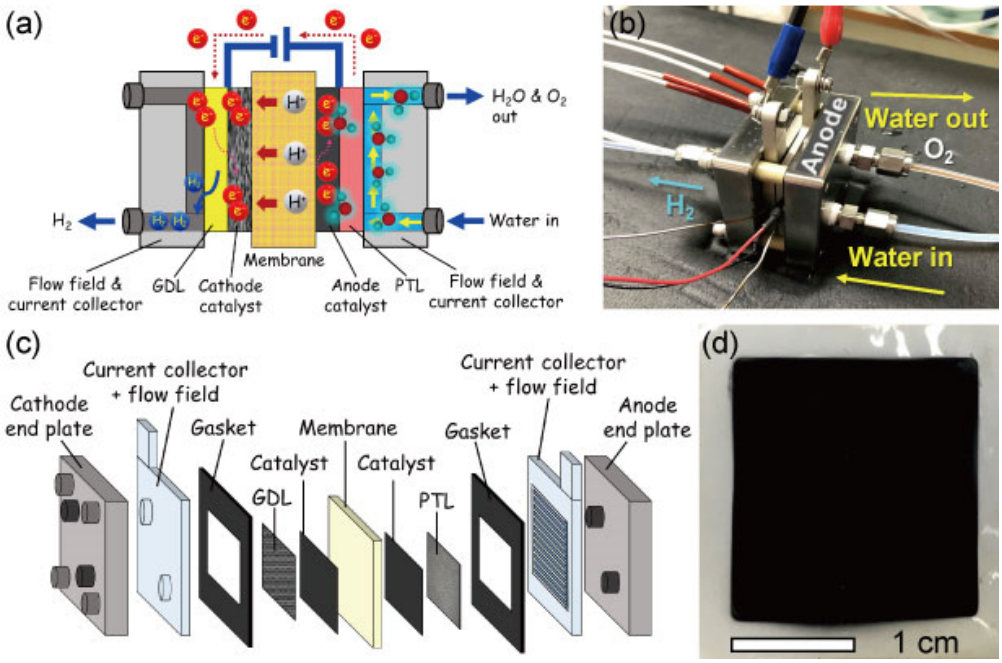

Supplementary Figure 12. Details of the PEM-type water electrolyzer. (a) Schematic illustration of PEM-type water electrolysis cell setup. (b) Optical image of the cell. (c) schematic illustration of the cell structures. (d) Optical image of the MEA. The assembly of the single-cell PEM water electrolyzer consisted of stainless steel (SUS316) endplates housing two titanium blocks (4.0×4.0×2.0 cm^3) that served as current collectors. Straight flow type fields with 4.0 cm^2 area were engraved into the current collectors. The channels of the flow fields had width and depth of 1.0 mm, while the width of the lands was 1.0 mm. The temperature was maintained during the experiments using two heating rods mounted onto the endplates. Two thermocouples were situated at the center of the two current collectors to measure the cell temperature. Nylon patches (thickness: 2.0 mm) were sandwiched between the endplates and the current collectors to provide electronic insulation as well as equal distribution of compressive forces on the sealing and catalyst layers. The membrane-electrode assembly (MEA) was placed between the current collectors with a carbon mesoporous gas diffusion layer (GDL) on the cathode and a Pt/Ti mesh porous transport layer (PTL) on the anode. Two gaskets (thickness: 0.16 mm) placed on the anode-side PTL and one gasket placed on the cathode-side GDL were used for both sealing and insulation. These components were kept under compression with the help of nut/bolt assembly with M8 screws onto the endplates (4 bolts, 4 Nm torque). The flow-field plates acted as current collectors that connected the power supply cables to the cell.

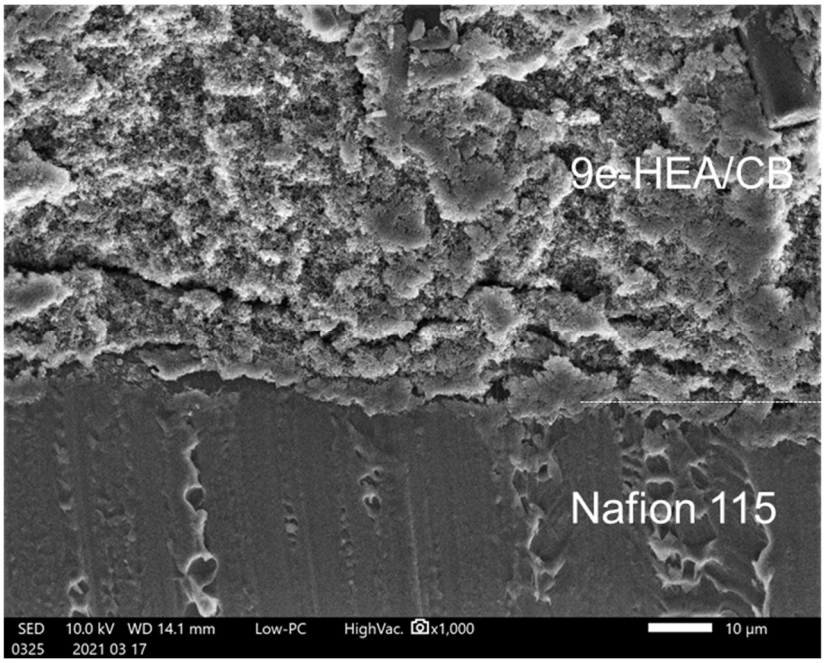

Supplementary Figure 13. Cross-sectional SEM image of MEA of 9eHEA/CB and Nafion 115 before tests.

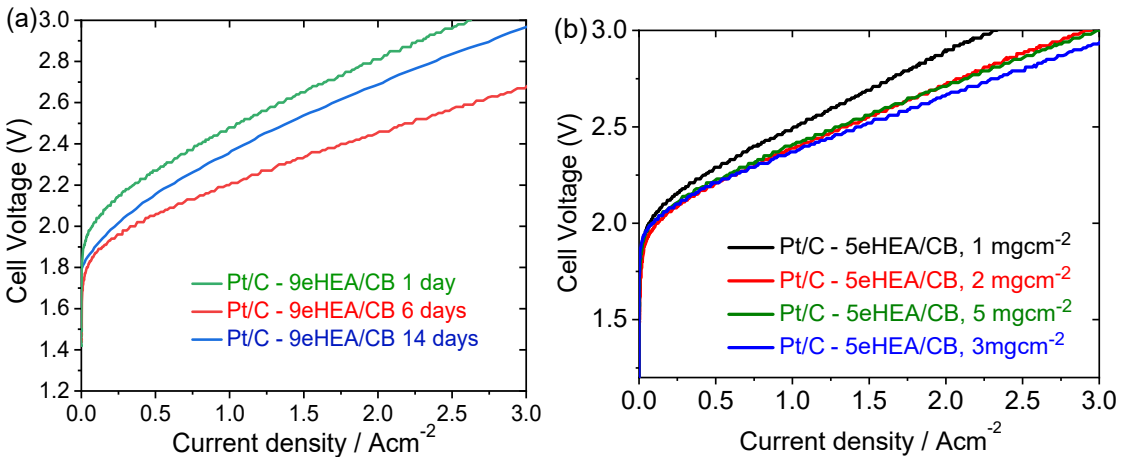

Supplementary Figure 14. Initial optimization of (a) catalyst ball milling time and (b) catalyst lording amount (60 rpm, 6 days ball milling) for IV curves (including iR). 1 day, 6 days and 14 days indicated the ball milling time.

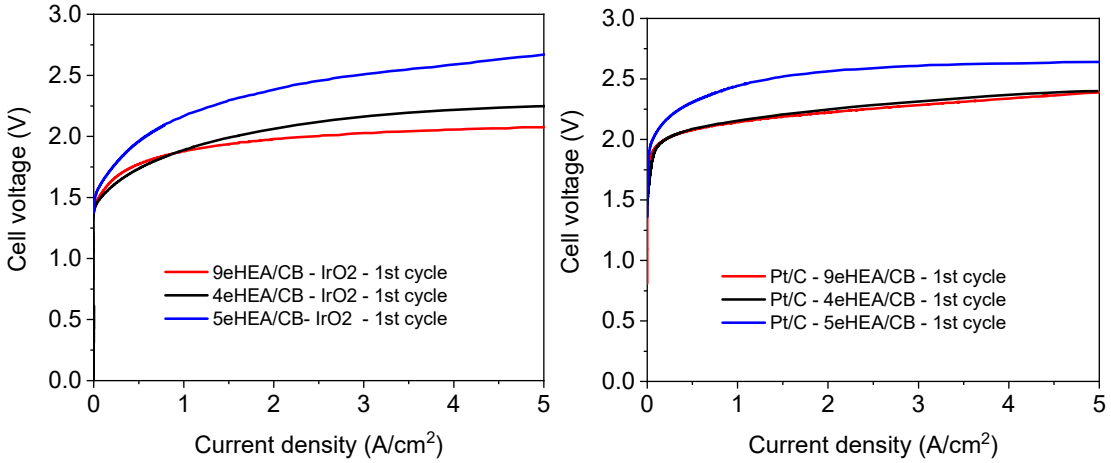

Supplementary Figure 15. IV curves of 4eHEA, 5eHEA and 9eHEA electrode. The current density was normalized by electrode surface area (4.0 cm^2).

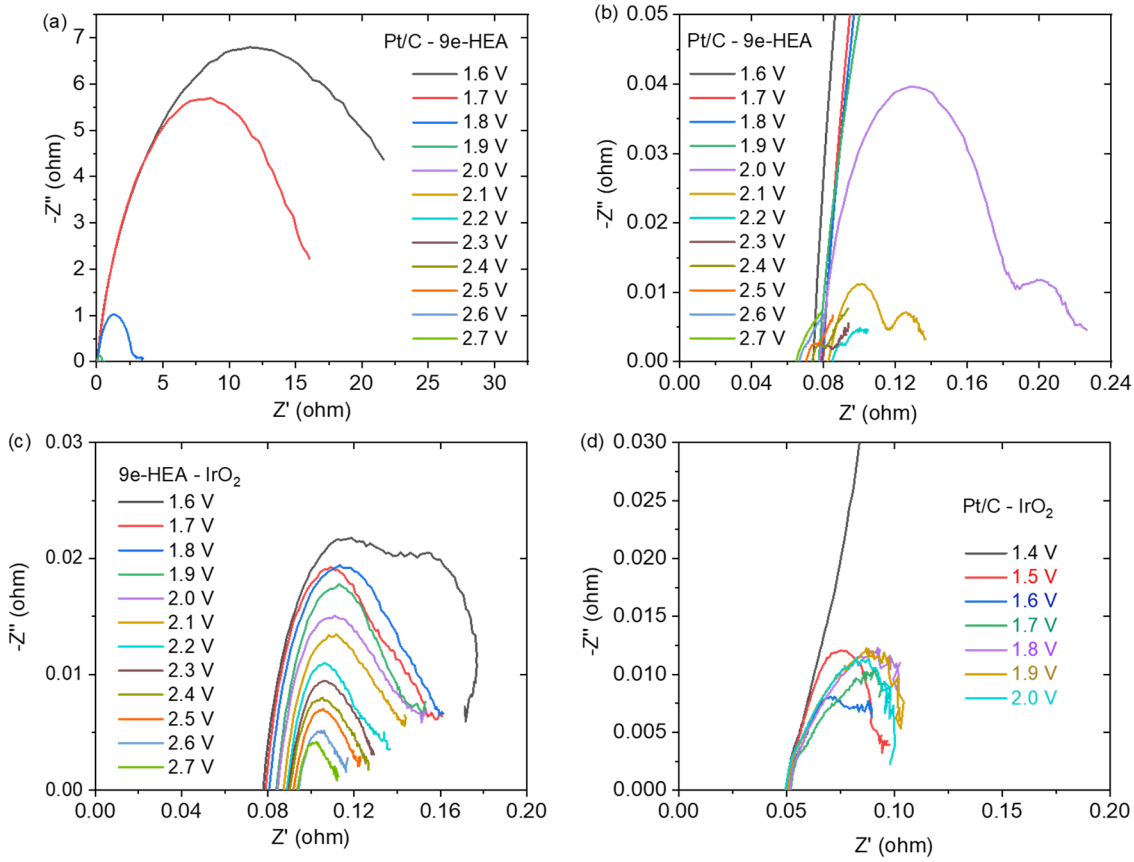

Supplementary Figure 16. Electrical impedance spectra of (a,b) 9eHEA anode, (c) 9eHEA cathode and (d) Pt/C-IrO_2. The Ormic resistance was 84 mΩ for 9eHEA-IrO_2 and 77 mΩ for Pt/C-9eHEA and charge transfer resistance was 52.9 mΩ for 9eHEA-IrO_2 and 100.6 mΩ for Pt/C-9eHEA at 2.0 V.

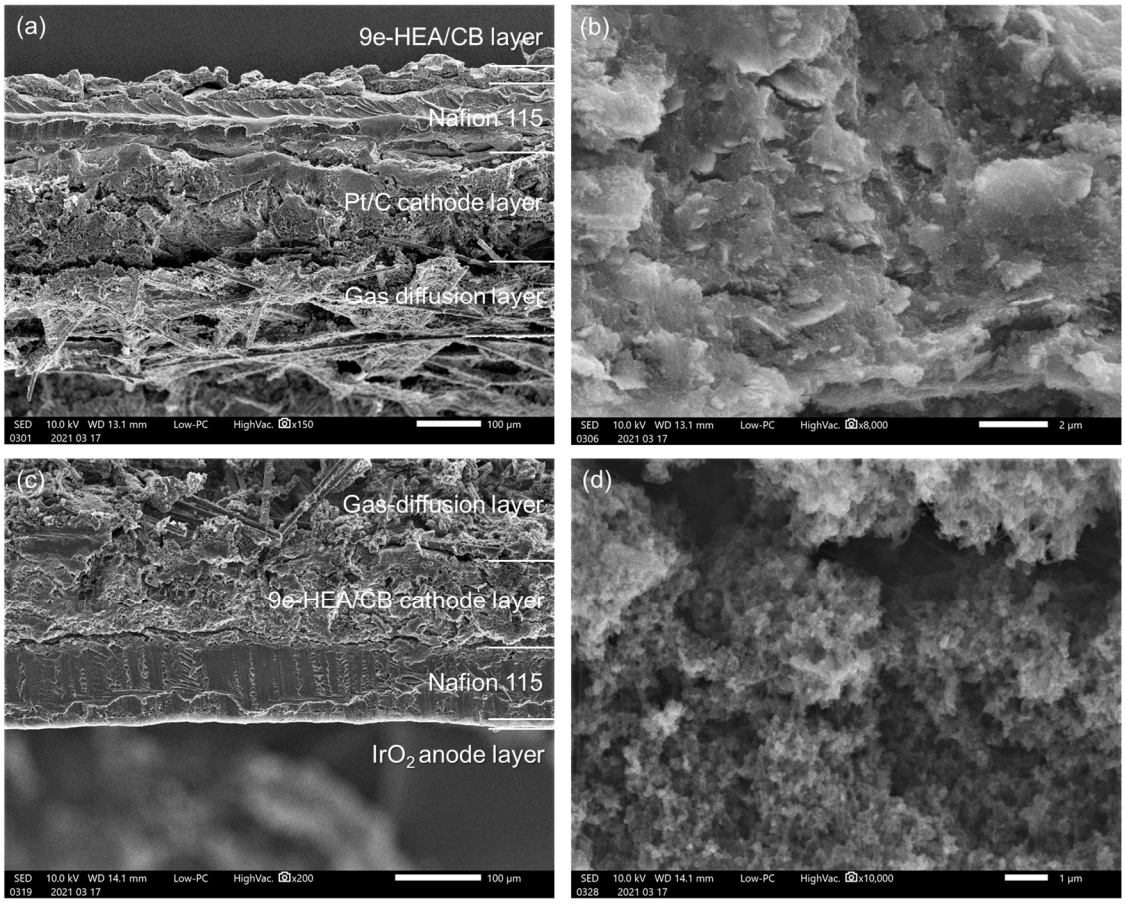

Supplementary Figure 17. Cross-sectional SEM images of MEA after the CA test for (a,b) anode and (c,d) cathode. Some catalyst layers were sticked on the GDL/PTL and then removed.

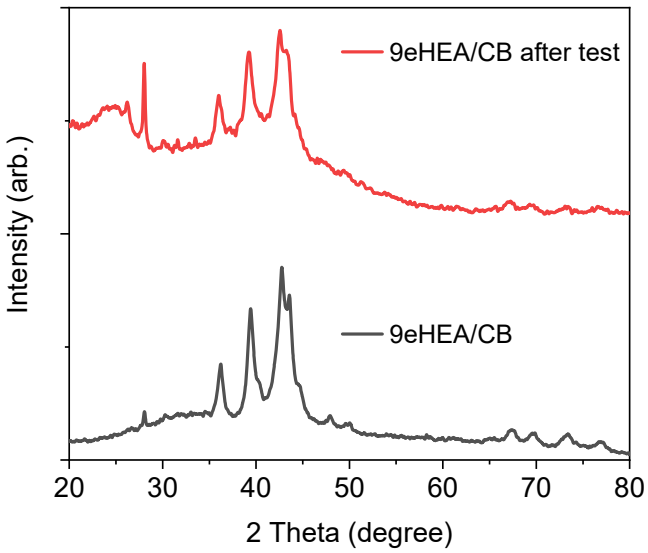

Supplementary Figure 18. XRD spectra of 9eHEA with carbon black (CB) anode before and after the CP test.

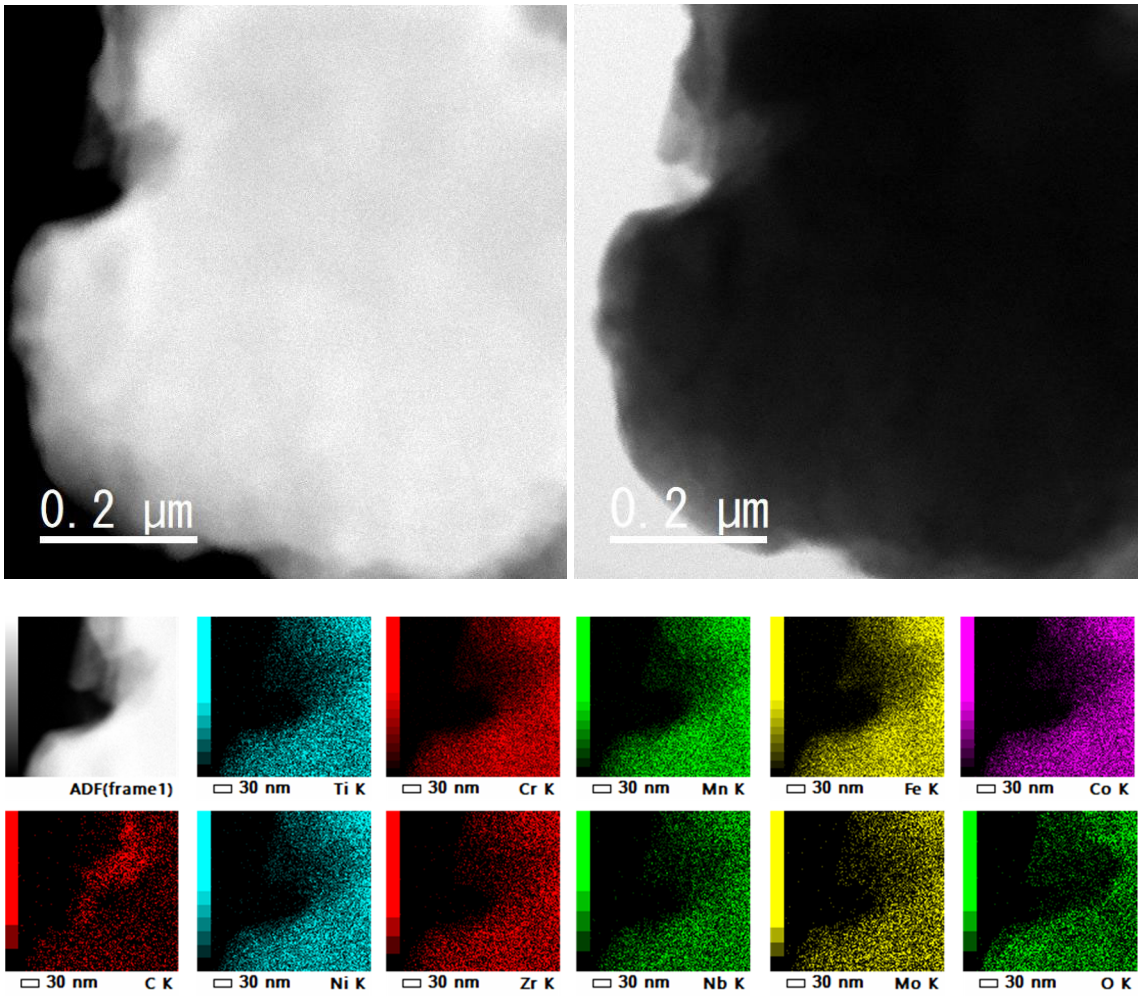

Supplementary Figure 19. Elemental mapping of 9eHEA/CB after the CP test by using STEM-EDX. C1s was assigned to residue Nafion as binders by XPS.

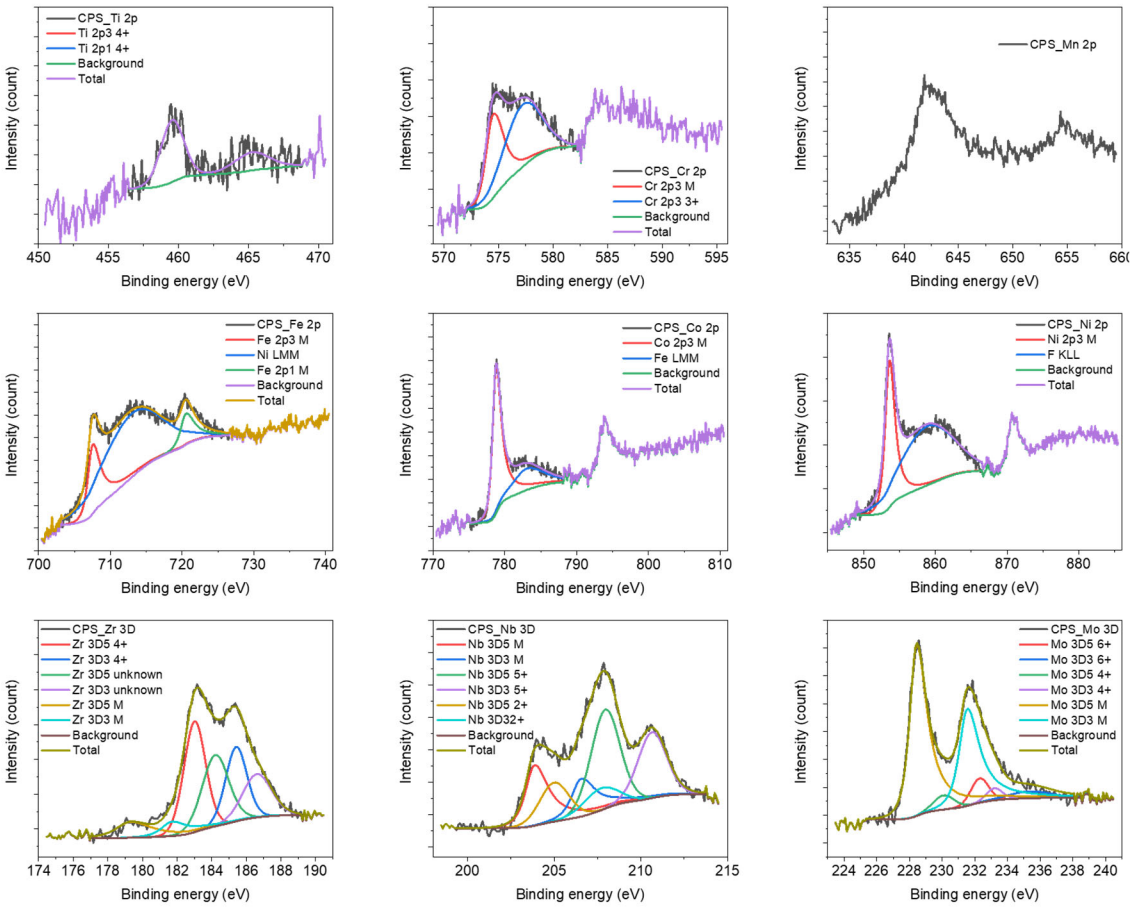

Supplementary Figure 20. XPS after the 100 hours CP test for cathode. The Nafion as binders could not completely removed and influenced the spectra.

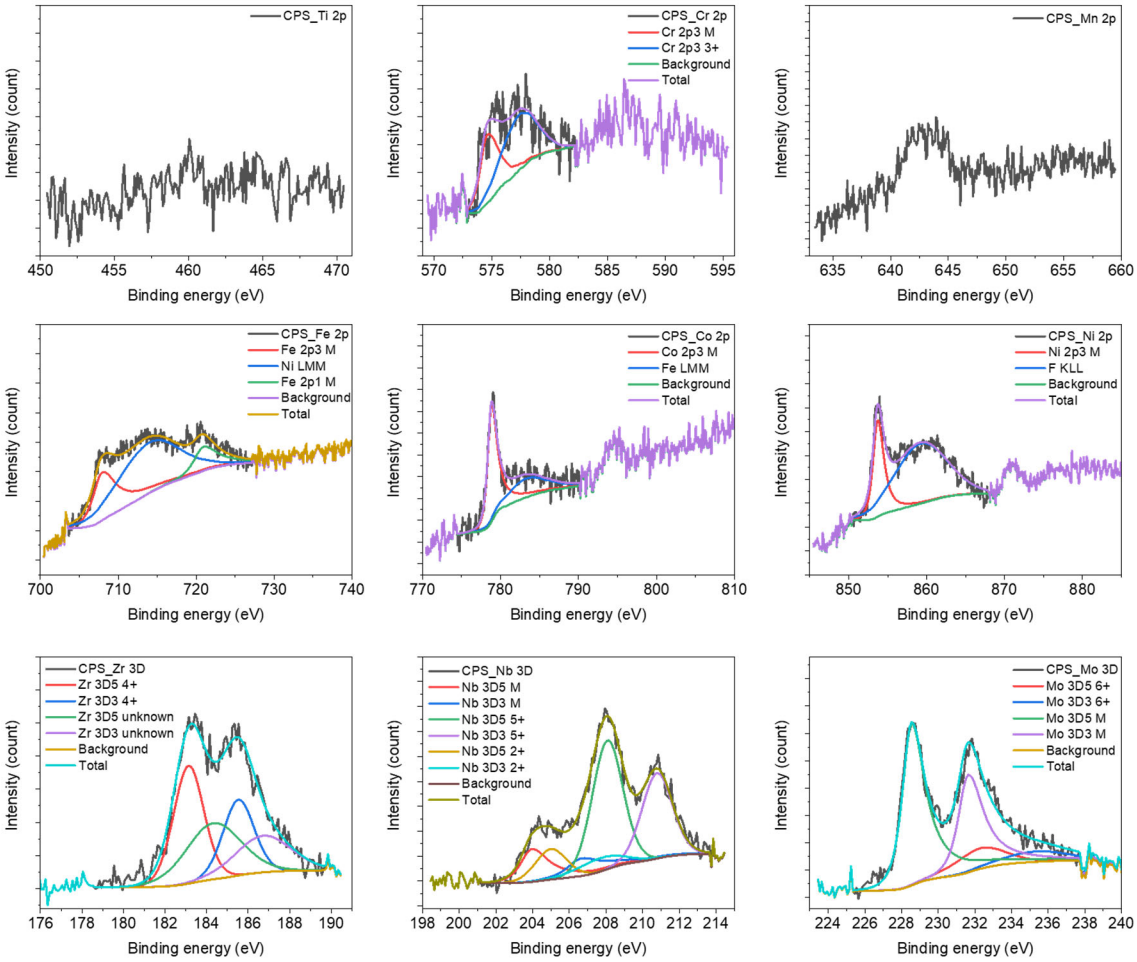

Supplementary Figure 21. XPS after 100 hours CP test for anode. The Nafion as binders could not completely removed and influenced the spectra.

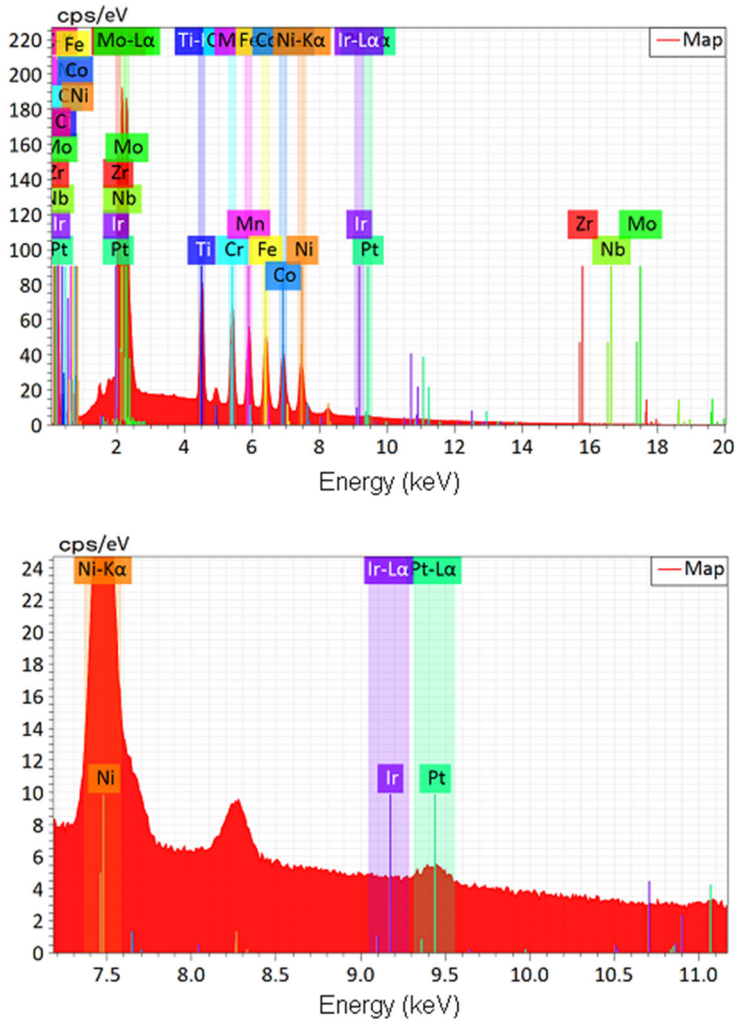

Element	9eHEAbefore CP test (at.%)	9eHEA after CP test (at.%)
Mo	11.9	11.1
Nb	11.4	18.3
Zr	10.9	11.2
Co	12.3	9.4
Ni	11.8	9.5
Fe	11.6	10.3
Mn	8.3	8.7
Cr	11.0	11.1
Ti	10.8	10.4
Ir	0	0

Supplementary Figure 22. SEM-EDX of MEA for Pt/C (cathode) - 9eHEA (anode) with the composition changes.

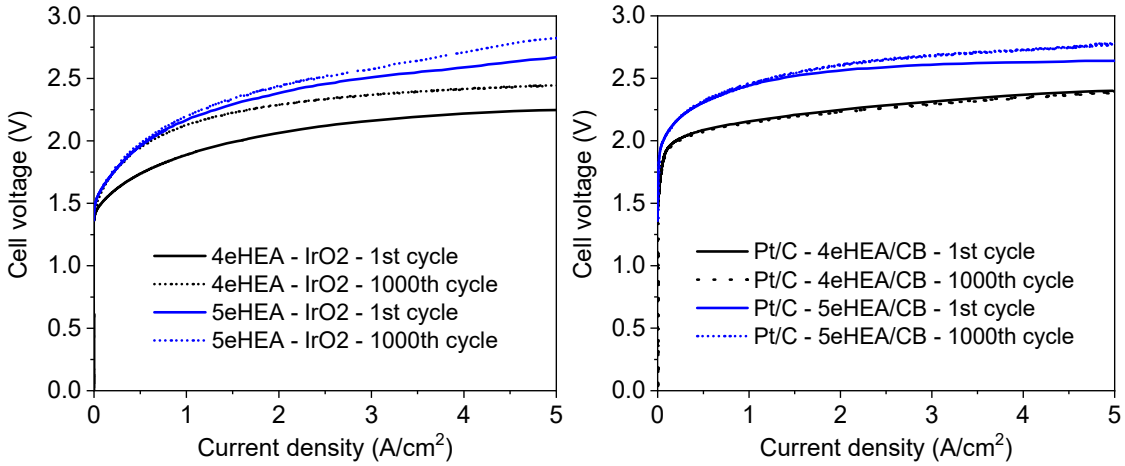

Supplementary Figure 23. Cycling stability of 4eHEA and 5eHEA cathode and anode. The current density was normalized by electrode surface area (4.0 cm^2).

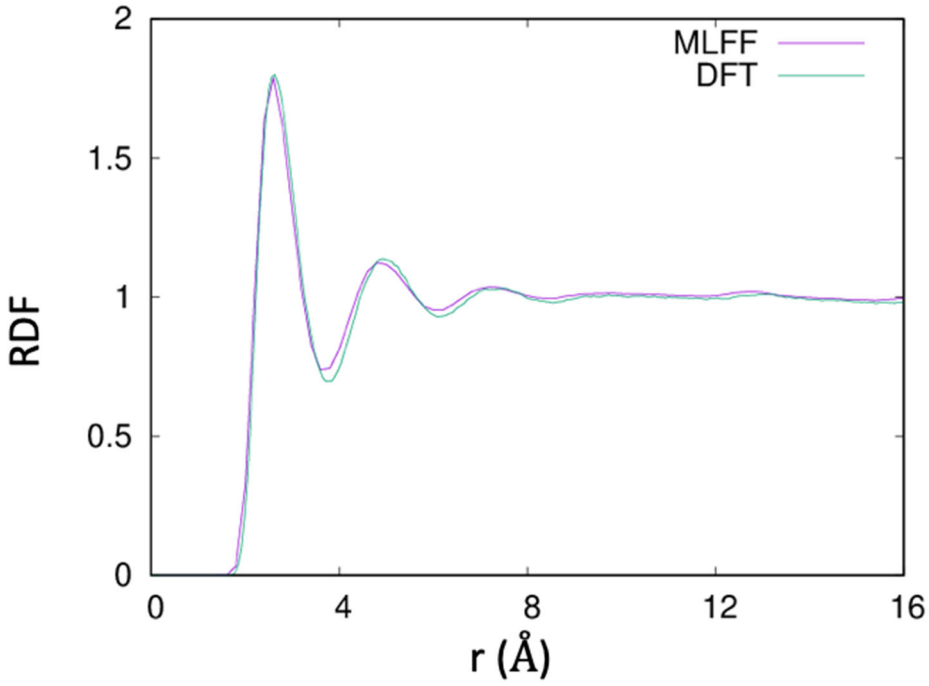

Supplementary Figure 24. Comparison of radial distribution function (RDF) calculate by MLFF-MD and DFT-MD simulations.

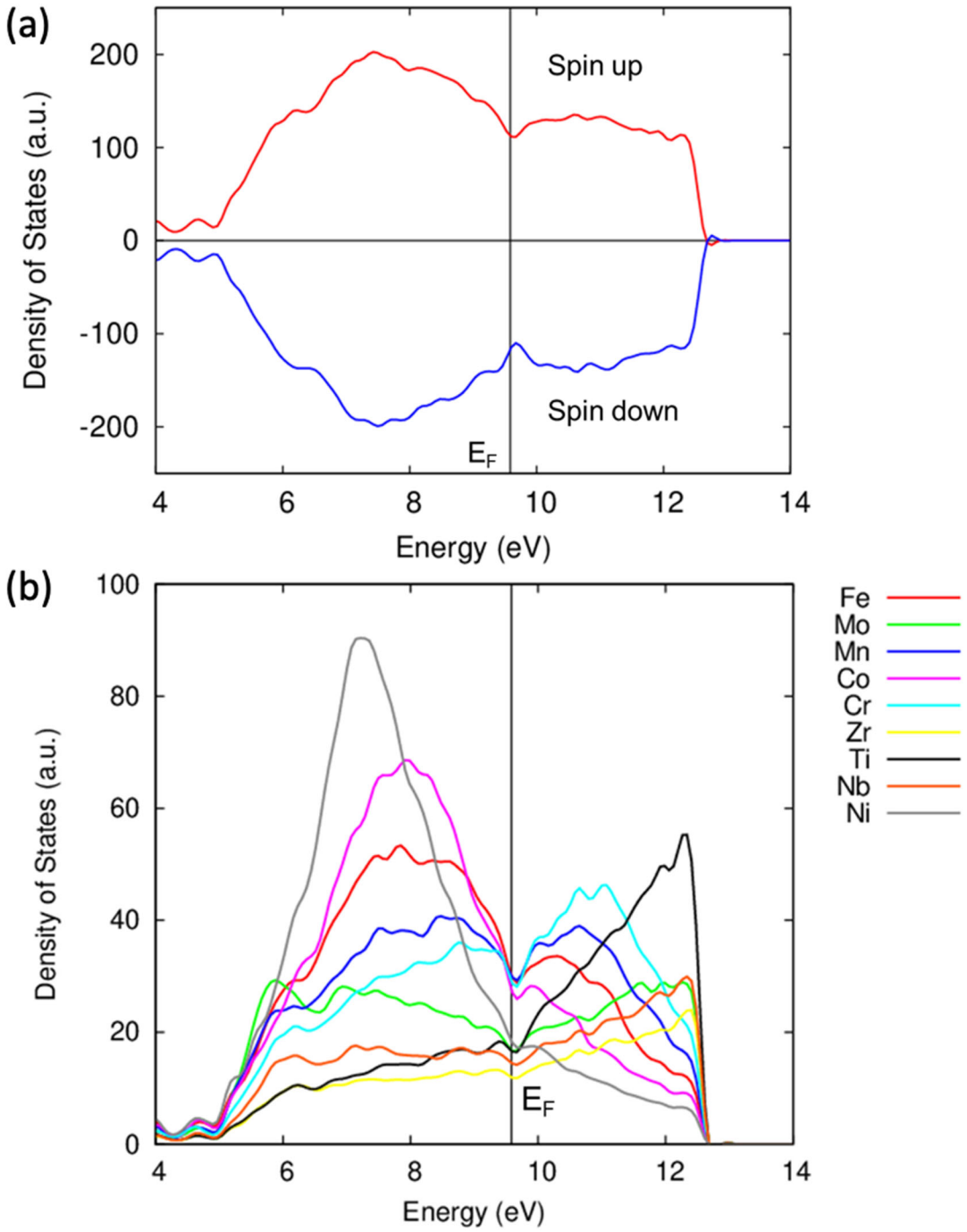

Supplementary Figure 25. (a) Total spin-resolved and (b) projected density of states of a bulk 9eHEA structure.

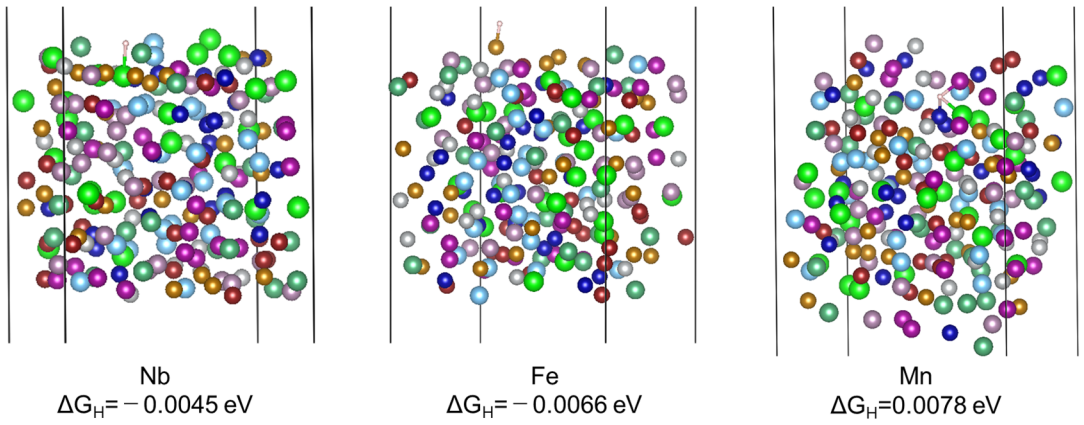

Supplementary Figure 26. Top 3 hydrogen adsorption sites for HER on 9eHEA. Red and white balls represent O and H atoms, respectively.

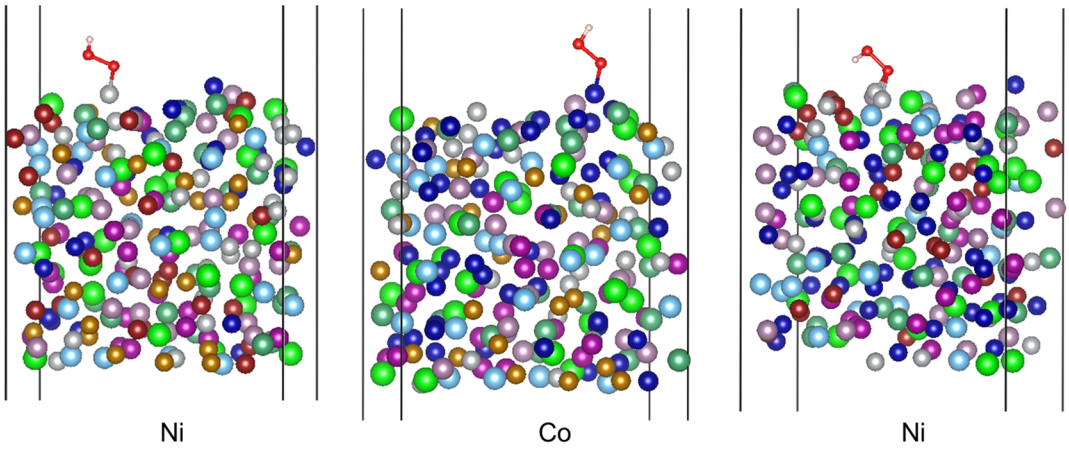

Supplementary Figure 27. Top 3 OOH adsorption sites for OER on 9eHEA. Red and white balls represent O and H atoms, respectively. The ΔG_{O^*} values in the Fig. 4(c) were −1.00 eV (Ni), −1.98 eV (Co), and −2.01 eV (Ni), respectively.

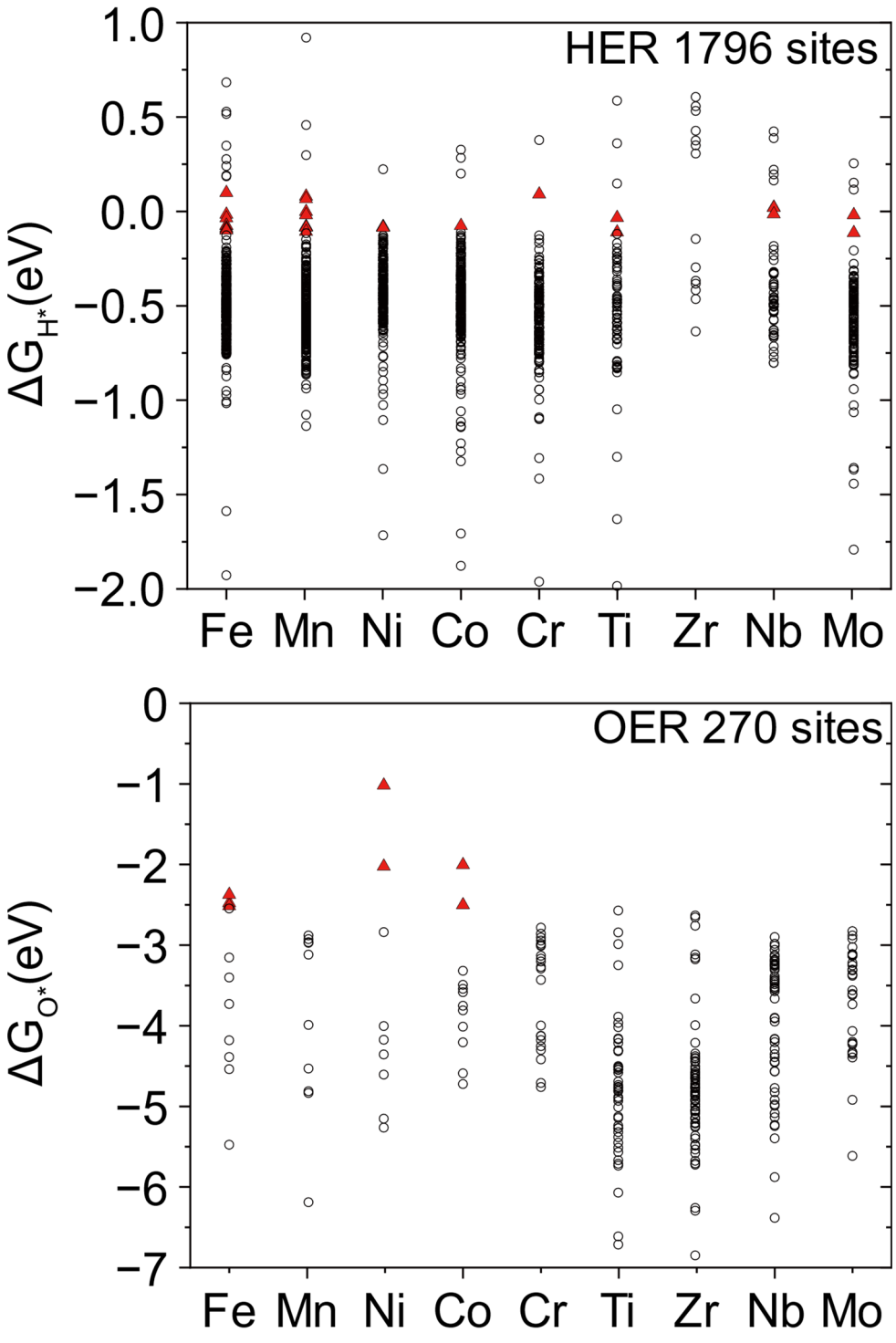

Supplementary Figure 28. Gibbs free energy profiles on the Ni with and without oxidation under an applied potential of 1.23 V in Figure 4b-c as magnified figures.

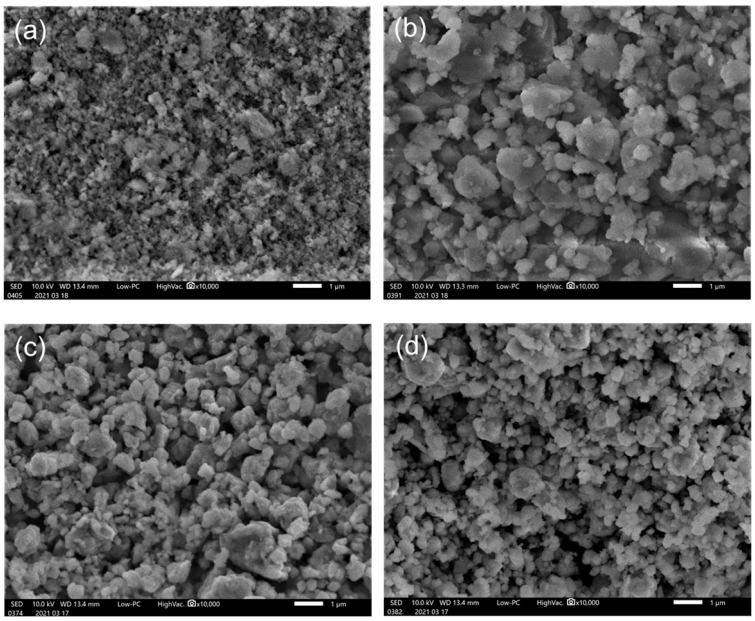

Supplementary Figure 29. SEM images of (a) 5eHEA, (b) 6eHEA, (c) 7eHEA and (d) 8eHEA.

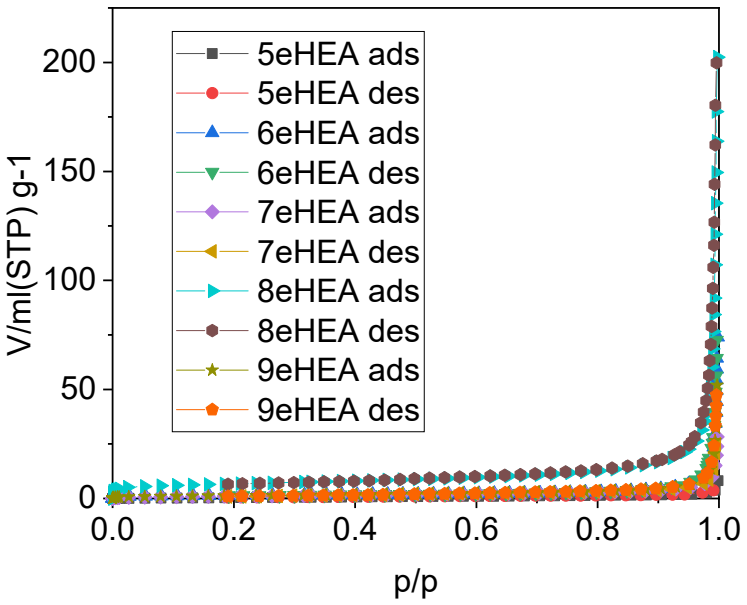

	5eHEA	6eHEA	7eHEA	8eHEA	9eHEA
BET surface area (m^2/g)	2.40	5.07	4.54	23.81	4.71

Supplementary Figure 30. Nitrogen adsorption and desorption. Adsorption isotherm of 5eHEA, 6eHEA, 7eHEA, 8eHEA and 9eHEA with their BET surface area.

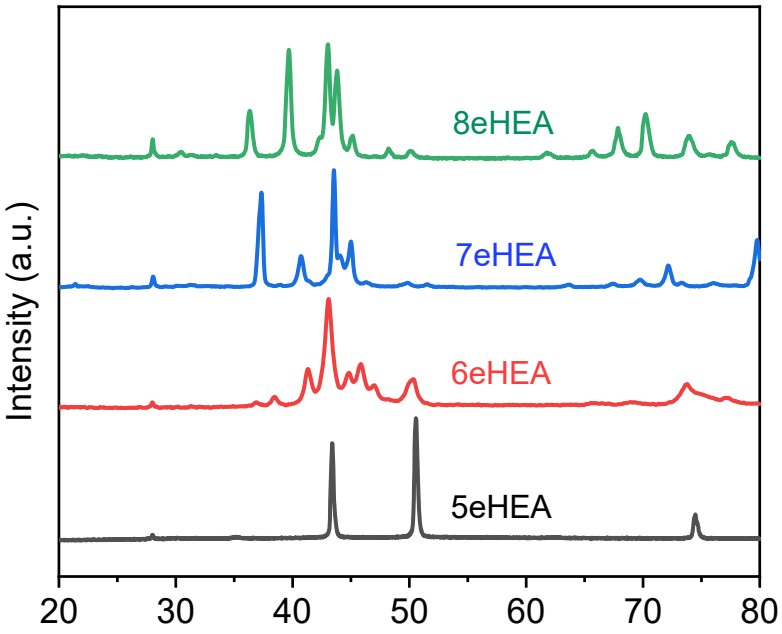

Supplementary Figure 31. XRD spectra of 5eHEA, 6eHEA, 7eHEA and 8eHEA.

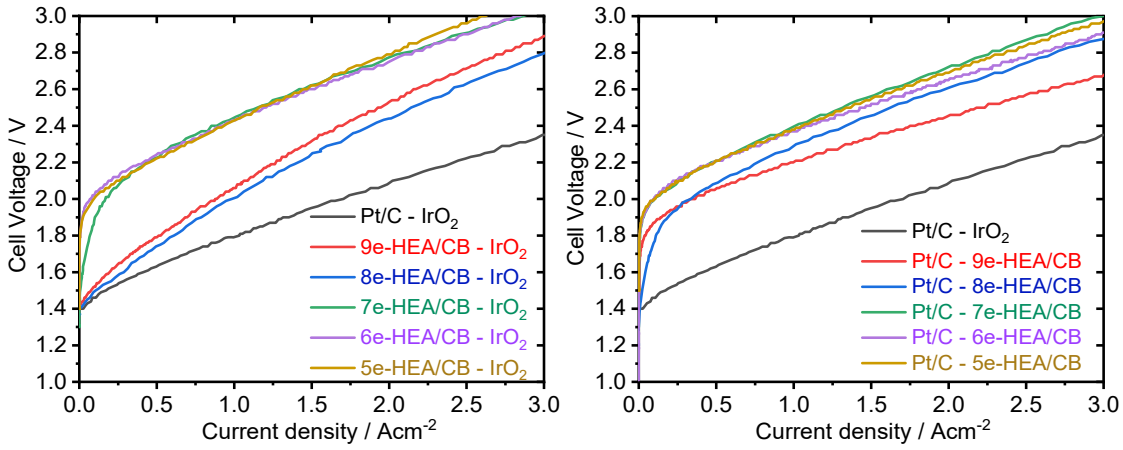

Supplementary Figure 32. IV-curve of PEM-type water electrolysis with5eHEA, 6eHEA, 7eHEA, 8eHEA and 9eHEA cathode and anode. The enhancement of 8eHEA could be attributed to 10 times higher BET surface area than other HEAs. The current density is normalised by the electrode surface area (4.0 cm^2).

Supplementary Table 1. Summary of elemental analysis by X-ray Fluorescence.

Element	9eHEA (at.%)	5eHEA (at.%)	4eHEA (at.%)
Mo	11.9	N/A	22.7
Nb	11.4	N/A	24.3
Zr	10.9	N/A	28.5
Co	12.3	20.8	N/A
Ni	11.8	20.0	N/A
Fe	11.6	19.8	N/A
Mn	8.3*	21.9	N/A
Cr	11.0	17.4	N/A
Ti	10.8	N/A	24.5

* Mn was evaluated during arc melting.

Supplementary Table 2. Summary of corrosion properties in 0.5 M H_2SO_4 at 25°C.

Sample	Anodic/cathodic E_{coor} (mV vs. SHE)	Anodic/cathodic I_{coor}(μA/cm^2)	Reference
9e-HEA	107/455	1.26/1.55	This work
5e-HEA	−144/489	1.82/1.51	This work
4e-HEA	5.07/519	1.75/0.71	This work
Bulk (poly)Pt	810/1480	0.063/0.013	8
Pt NPs/carbon	500/1550	100/25	9
PtNi-NPs	400/1520	14/6.3	10
PtCo-NPs	470/1560	25/16	10
$CrFe_{1.5}MnNi_{0.5}$	−229/N.A	686/N.A	11
$Al_{0.3}CrFe_{1.5}MnNi_{0.5}$	−194/N.A	2390/N.A	11
$Al_{0.5}CrFe_{1.5}MnNi_{0.5}$	−206/N.A	5080/N.A	11
304 stainless steel	−186/N.A or −185/N.A	74.5/N.A or 45.3/N.A	11 or 12
Bulk Ni	−92.3/N.A	27.46/N.A	13
Bulk Cu	225/N.A	22.5/N.A	14
Bulk Fe	−280/N.A	200/N.A	15
$Ni_{71}P_{29}$	216/N.A	3.1/N.A	13
$Ni_{78}W_9P_{13}$	200/N.A	6.8/N.A	13
$Ni_{79}Mo_{14}P_7$	194/N.A	8.3/N.A	13
CoCrFeNi	−81/N.A	15.8/N.A	12
$Al_{0.25}CoCrFeNi$	−95/N.A	16.7/N.A	12
$Al_{0.50}CoCrFeNi$	−84/N.A	13.4/N.A	12
AlCoCrFeNi	−94/N.A	13.1/N.A	12
$Co_{1.5}CrFeNi_{1.5}Ti_{0.5}$	−92/N.A	30/N.A	16
$Co_{1.5}CrFeNi_{1.5}Ti_{0.5}Mo_{0.1}$	−71/N.A	78/N.A	16
$Co_{1.5}CrFeNi_{1.5}Ti_{0.5}Mo_{0.5}$	−64/N.A	72/N.A	16
$Co_{1.5}CrFeNi_{1.5}Ti_{0.5}Mo_{0.8}$	−70/N.A	69/N.A	16

Supplementary Table 3. Summary of XPS for each element on 9eHEA. “Pristine” and “Metallic” means the state after the mirror-finished and Ar ion etching (cleaning of carbon contamination) and after further removal of oxides on the surface, respectively.

	Normalized Intensity			Binding Energy (eV)		
Ti	Metal	TiO_2	TiO_x	Metal	TiO_2	TiO_x
Pristine	0.101	0.674	0.133	454.5	459.0	457.0
Metallic	0.644	0.000		454.5		
OCP	0.297	0.226		454.4	458.8	
0.92 V	0.051	0.429		454.4	458.6	
1.65 V	0.000	0.376			458.3	
1.90 V	0.000	0.410			457.9	
0.07 V	0.000	0.479			459.2	

	Normalized Intensity				Binding Energy (eV)			
Cr	Metal	$Cr(OH)_3$	CrO_3	Cr_2O_3	Metal	$Cr(OH)_3$	CrO_3	Cr_2O_3
Pristine	0.940	0.000	0.000	0.993	574.3			576.7
Metallic	1.324	0.000	0.000		574.1			
OCP	0.566	0.669	0.000		574.2	577.3		
0.92 V	0.000	0.429	0.000			577.2		
1.65 V	0.000	0.211	0.143			576.8	579.0	
1.90 V	0.000	0.000	0.302				578.8	
0.07 V	0.000	0.528	0.000			577.7		

	Normalized Intensity			Binding Energy (eV)		
Mn	Metal	Mn_2O_3	MnO_2	Metal	Mn_2O_3	MnO_2
Pristine	0.000	0.000	0.424			642.7
Metallic	0.397	0.000		638.9		
OCP	0.255	0.000		639.1		
0.92 V	0.000	0.108			641.6	
1.65 V	0.000	0.231			641.7	
1.90 V	0.000	0.288			641.6	
0.07 V	0.000	0.138			641.5	

Supplementary Table 3. Summary of XPS for each element on 9eHEA. (continued)

	Normalized Intensity		Binding Energy (eV)	
Fe	Metal	Fe_2O_3 and/or Fe_3O_4	Metal	Fe_2O_3 and/or Fe_3O_4
Pristine	0.603		707.0	
Metallic	1.493	0.000	707.0	
OCP	0.493	0.000	707.0	
0.92 V	0.036	0.528	706.6	710.9
1.65 V	0.000	0.360		711.4
1.90 V	0.000	0.427		710.6
0.07 V	0.000	0.214		710.3

	Normalized Intensity			Binding Energy (eV)		
Co	Metal	$Co(OH)_2$	CoO	Metal	$Co(OH)_2$	CoO
Pristine	0.620			778.4		
Metallic	1.731	0.000	0.000	778.4		
OCP	0.610	0.000	0.000	778.3		
0.92 V	0.071	0.473	0.000	778.4	781.7	
1.65 V	0.000	0.000	0.289			780.8
1.90 V	0.000	0.000	0.374			780.6
0.07 V	0.000	0.165	0.000		781.7	

	Normalized Intensity			Binding Energy (eV)		
Ni	Metal	$Ni(OH)_2$	NiO	Metal	$Ni(OH)_2$	NiO
Pristine	1.216			853.1		
Metallic	1.610	0.000	0.000	853.1		
OCP	0.774	0.000	0.000	853.0		
0.92 V	0.052	0.704	0.000	853.3	856.9	
1.65 V	0.000	0.000	0.213			855.6
1.90 V	0.000	0.000	0.336			855.6
0.07 V	0.000	0.127	0.000		856.6	

Supplementary Table 3. Summary of XPS for each element on 9eHEA. (continued)

	Normalized Intensity			Binding Energy (eV)		
Zr	Metal	ZrO_2-A	ZrO_2-B	Metal	ZrO_2-A	ZrO_2-B
Pristine	0.163	1.050			182.6	
Metallic	0.833	0.000	0.000	179.2		
OCP	0.391	0.368	0.102	179.2	182.5	183.8
0.92 V	0.094	0.574	0.160	178.9	182.3	183.9
1.65 V	0.026	0.601	0.176	178.9	182.0	183.1
1.90 V	0.000	0.728	0.000		181.8	
0.07 V	0.010	0.543	0.219	179.0	182.7	184.1

	Normalized Intensity			Binding Energy (eV)		
Nb	Metal	Nb_2O_5	NbO	Metal	Nb_2O_5	NbO
Pristine	0.284	0.456	0.259	203.1	207.5	204.3
Metallic	1.000	0.000		203.1		
OCP	0.534	0.466		203.1	207.5	
0.92 V	0.105	0.895		203.2	207.4	
1.65 V	0.018	0.982		203.1	206.9	
1.90 V	0.000	1.000			206.6	
0.07 V	0.010	0.990		203.1	207.9	

	Normalized Intensity			Binding Energy (eV)		
Mo	Metal	MoO_2	MoO_3	Metal	MoO_2	MoO_3
Pristine	0.853			227.9		
Metallic	1.196	0.000	0.000	227.7		
OCP	0.561	0.436	0.000	227.8	228.9	
0.92 V	0.000	0.579	0.185		228.4	232.8
1.65 V	0.000	0.012	0.380		228.9	232.3
1.90 V	0.000	0.000	0.351			232.0
0.07 V	0.000	0.000	0.297			232.6

Supplementary Table S4. Summary of molar percent (mol%) with and without O from O1s spectra estimated by EC-XPS during the OER process at OCP, 0.92 V, 1.65 V, 1.90 V and 0.07 V after the OER. “Metallic” means the state after further removal of oxides on the surface.

	Zr	Nb	Mo	Ti	Cr	Mn	Fe	Co	Ni	O from O1s
Metallic	8.1	9.8	11.7	6.5	12.9	3.9	14.6	16.9	15.7	N/A
	8.1	9.7	11.6	6.5	12.9	3.9	14.5	16.8	15.6	0.4
OCP	12.7	14.8	14.7	8.0	18.2	3.8	7.3	9.0	11.4	N/A
	9.6	11.1	11.1	6.0	13.7	2.8	5.5	6.8	8.6	24.7
0.92 V	13.8	16.7	12.7	8.3	15.7	1.8	9.4	9.1	12.6	N/A
	9.4	11.4	8.7	5.7	10.7	1.2	6.4	6.2	8.6	31.5
1.65 V	19.9	24.8	9.7	9.7	8.8	5.7	8.9	7.2	5.3	N/A
	10.4	13.0	5.1	5.1	4.6	3.0	4.7	3.8	2.8	47.6
1.90 V 45°	17.2	23.6	8.3	10.0	7.1	6.8	10.1	8.8	7.9	N/A
	10.1	13.9	4.9	5.9	4.2	4.0	5.9	5.2	4.7	41.3
1.90 V 75°	20.1	29.1	6.1	7.2	5.3	3.4	6.6	12.4	9.7	N/A
	11.4	16.5	3.4	4.1	3.0	1.9	3.8	7.0	5.5	43.4
0.07 V	20.7	26.8	8.0	13.3	14.1	3.7	5.7	4.4	3.4	N/A
	14.2	18.4	5.5	9.1	9.7	2.5	3.9	3.0	2.3	31.2

Supplementary Table 5. Summary of PEM performance on the reported anodes and cathodes. The cycling durability was checked at 5.0 A/cm^2.

Catalyst	Test conditions	Overpotential at 1.0 A/cm^2	Cycling durability	Reference
9eHEA	Cell: 80°C Water: 10 ml/min	2.14 V (anode) 1.88 V (cathode)	No degradation 5.4% reduction	This work
5eHEA	Cell: 80°C Water: 10 ml/min	2.4 V (anode) 2.1 V (cathode)	9.8% reduction 7.8% reduction	This work
4eHEA	Cell: 80°C Water: 10 ml/min	2.1 V (anode) 1.9 V (cathode)	No degradation 10.3% reduction	This work
IrO_2/N-CN (anode catalyst)	Cell: 80°C Water: 30 ml/min	1.65 V (iR-contained)	N/A	17
TiO_2-IrO_2 (anode catalyst)	Cell: 80°C Water: 5 ml/min	1.64 V (iR-contained)	N/A	18
Pt@IrO_2 (anode catalyst)	Cell: 80°C Water: 15 ml/min	1.55 V (iR-contained)	N/A	19
RuO_2@IrO_x core-shell nanocomposite (anode catalyst)	Cell: 80°C Water: 40 ml/min	1.68 V (iR-contained)	N/A (CA test only)	20
Magnetized IrO_2-Fe_3O_4 (anode catalyst)	Cell: 80°C Water: 100 ml/min	2.40 V (iR-contained)	N/A	21
IrO_2/ATO (anode catalyst)	Cell: 80°C Water: 3 ml/min	1.63 V (iR-contained)	N/A	22
IrO_x/W-TiO_2 (anode catalyst)	Cell: 80°C Water: N/A	1.56 V	N/A (CA test only)	23
$Co((Pntr(CH_2)_3S)_2Gm)_3(BC_6H_5)_2$ (cathode catalyst)	Cell: 80°C Water: N/A	2.03 V (iR-contained)	N/A	24
Co_3O_4 (cathode catalyst)	Cell: 80°C Water: 0.5 mL/min	2.25 V (iR-contained)	N/A (CA test only)	25
Pd/B_3–CNPs (cathode catalyst)	Cell: 80°C Water: 60 mL/min	2.04 V (iR-contained)	N/A (CA test only)	26
RuS_2@MoS_2 (cathode catalyst)	Cell: 80°C Water: 40 mL/min	1.68 V (iR-contained)	N/A	27
$Ni_{78}P_{22}$ (cathode catalyst)	Cell: 90°C Water: 15 mL/min	1.96 V (iR-contained)	N/A	28
$Fe(Cl_2Gm)_3(BC_6H_5)_2$ (cathode catalyst)	Cell: 80°C Water: N/A	2.10 V (iR-contained)	N/A	29
Graphene-encapsulated NiMo (cathode catalyst)	Cell: 80°C Water: 10 ml/min	2.00 V (iR-contained)	No degradation	30

Supplementary Table 6. DFT-calculated Gibbs free energy of H* on the HER processes.

	$\lvert\Delta G_{H^*}\rvert \leq 0.1$ eV		$\lvert\Delta G_{H^*}\rvert \leq 0.3$ eV	
Element	**Number of sites**	**Average**	**Number of sites**	**Average**
Fe	8	0.0190	29	0.175
Mo	2	0.00698	17	0.188
Mn	3	0.00246	29	0.158
Co	3	0.0248	31	0.203
Cr	7	0.0633	42	0.186
Zr	0	N.A	14	0.163
Ti	0	N.A	25	0.158
Nb	2	0.00549	14	0.195
Ni	1	0.0260	23	0.162

Supplementary Table 7. DFT-calculated Gibbs free energy of $\max\Delta G(\{\lvert\Delta G_{OH^*}\rvert, \lvert\Delta G_{O^*}\rvert, \lvert\Delta G_{OOH^*}\rvert\}-1.23)$ on the OER processes.

	$\lvert\max\Delta G - 1.23\rvert \leq 2.0$ eV		$\lvert\Delta G_{O^*}\rvert \leq 2.5$ eV	
Element	**Number of sites**	**Average**	**Number of sites**	**Average**
Fe	7	1.73	4	2.44
Mo	5	1.84	0	N.A
Mn	10	1.72	0	N.A
Co	2	1.89	2	2.23
Cr	10	1.84	0	N.A
Zr	1	1.19	0	N.A
Ti	0	N.A	0	N.A
Nb	1	1.72	0	N.A
Ni	2	1.81	2	1.50

Supplementary Table8. Summary of elemental analysis by X-ray Fluorescence for 5eHEA, 6eHEA, 7eHEA and 8eHEA.

Element	5eHEA (at.%)	6eHEA (at.%)	7eHEA (at.%)	8eHEA (at.%)
Mo	N/A	26.8	20.0	18.2
Nb	N/A	N/A	18.6	16.2
Zr	N/A	N/A	N/A	14.7
Co	20.8	15.7	12.9	11.2
Ni	20.0	15.2	12.8	10.7
Fe	19.8	14.7	12.3	10.4
Mn	21.9	15.0	12.8	9.6
Cr	17.4	12.7	10.6	9.0

* Mn was evaluated during arc melting.

References

1 Wang Y, *et al.* Study of oxygen evolution reaction on amorphous $Au_{13}@Ni_{120}P_{50}$ nanocluster. *Physical Chemistry Chemical Physics*, 14545-14556 (2018).

2 Seitz LC, *et al.* A highly active and stable $IrO_x/SrIrO_3$ catalyst for the oxygen evolution reaction. *Science*, 1011-1014 (2016).

3 Unke OT, *et al*. Machine Learning Force Fields. *Chemical Reviews,*10142–10186 (2021).

4 Jinnouchi R, *et al.* Phase transitions of hybrid perovskites simulated by machine-learning force fields trained on the fly with Bayesian inference. *Physical Review Letters,* 225701 (2019).

5 Bartók AP, *et al.* Gaussian approximation potentials: the accuracy of quantum mechanics, without the electrons. *Physical Review Letters,* 136403 (2010).

6 Bartók AP, *et al.* On representing chemical environments. *Physical Review B,* 184115 (2013).

7 Brundle CR, *et al.* X-ray photoelectron spectroscopy: A perspective on quantitation accuracy for composition analysis of homogeneous materials. *Journal of Vacuum Science & Technology A,* 041001 (2020).

8 Tahmasebi S, *et al.* Corrosion behaviour of platinum in aqueous H_2SO_4 solution: part 1 – influence of the potential scan rate and the dissolved gas. *Electrocatalysis,* 172 – 181 (2018).

9 Tahmasebi S, *et al.* How stable are spherical platinum nanoparticles applied to fuel cells? *The Journal of Physical Chemistry C,* 11765 – 11776 (2018).

10 Tahmasebi S, *et al.* Oxidation and corrosion of platinum-nickel and platinum-cobalt nanoparticles in an aqueous acidic medium. *ACS Applied Energy Materials,* 7019 – 7035 (2019).

11 Lee CP, *et al.* Effect of the aluminium content of $Al_xCrFe_{1.5}MnNi_{0.5}$ high-entropy alloys on the corrosion behaviour in aqueous environments. *Corrosion Science,* 2053 – 2060 (2008).

12 Kao YF, *et al.* Electrochemical passive properties of $Al_xCoCrFeNi$ (x = 0, 0.25, 0.50, 1.00) alloys in sulfuric acids. *Corrosion Science,* 1026 – 1034 (2010).

13 Lu G, *et al.* Corrosion resistance of ternary Ni–P based alloys in sulfuric acid solutions. *Electrochimica Acta,* 2969 – 2979 (2002).

14 Quartarone G, *et al.* Inhibition of copper corrosion by isatin in aerated 0.5 M H_2SO_4. *Corrosion Science,* 715 – 733 (2003).

15 Lorenz WJ. Determination of corrosion rates by electrochemical DC and AC methods. *Corrosion Science,* 647 – 672 (1981).

16 Chou YL, *et al.* The effect of molybdenum on the corrosion behaviour of the high-entropy alloys $Co_{1.5}CrFeNi_{1.5}Ti_{0.5}Mo_x$ in aqueous environments. *Corrosion Science,* 2571 – 2581 (2010).

17 Wang S, *et al.* Defect engineering assisted support effect: IrO_2/N defective g-C_3N_4 composite as highly efficient anode catalyst in PEM water electrolysis. *Chemical Engineering Journal,* 129455 (2021).

18 Böhm D, *et al.* Highly conductive titania supported iridium oxide nanoparticles with

low overall iridium density as OER catalyst for large-scale PEM electrolysis. *Applied Materials Today,* 101134 (2021).

19 Lim A, *et al.* Low-loading IrO_2 supported on Pt for catalysis of PEM water electrolysis and regenerative fuel cells. *Applied Catalysis B: Environmental,* 118955 (2020). .

20 Lv H, *et al.* Self-assembled RuO_2@IrO_x core-shell nanocomposite as high efficient anode catalyst for PEM water electrolyzer. *Applied Surface Science,* 145943 (2020).

21 Kaya MF, *et al.* Magnetically modified electrocatalysts for oxygen evolution reaction in proton exchange membrane (PEM) water electrolyzers. *International Journal of Hydrogen Energy,* 20825 – 20834 (2021).

22 Han SB, *et al.* Mesoporous iridium oxide/Sb-doped SnO_2 nanostructured electrodes for polymer electrolyte membrane water electrolysis. *International Journal of Hydrogen Energy,* 1409 – 1416 (2020).

23 Min X, *et al.* High performance and cost-effective supported IrO_x catalyst for proton exchange membrane water electrolysis. *Electrochimica Acta,* 138391 (2021).

24 Pushkarev AS, *et al.* Electrocatalytic hydrogen production using the designed hexaphenanthrene iron, cobalt and ruthenium(II) cage complexes as cathode (pre) catalysts immobilized on carbonaceous substrates. *International Journal of Hydrogen Energy,* 26206 – 26216 (2020).

25 Ampurdanés J, *et al.* Cobalt-oxide based materials as non-PGM catalyst for HER in PEM electrolysis and *in situ* XAS characterization of its functional state. *Catalysis Today,* 161 – 168 (2018).

26 Kumar SS, *et al.* Boron-doped carbon nanoparticles supported palladium as an efficient hydrogen evolution electrode in PEM water electrolysis. *Renewable Energy,* 2281 – 2290 (2019).

27 Sarno M, *et al.* High hydrogen production rate on RuS_2@MoS_2 hybrid nanocatalyst by PEM electrolysis. *International Journal of Hydrogen Energy,* 4398 – 4405 (2018).

28 Kim H, *et al.* Pulse-electrodeposited nickel phosphide for high-performance proton exchange membrane water electrolysis. *Journal of Alloys and Compounds,* 296 – 304 (2019).

29 Grigoriev SA, *et al.* Hydrogen production by proton exchange membrane water electrolysis using cobalt and iron hexachloroclathrochelates as efficient hydrogen-evolving electrocatalysts. *International Journal of Hydrogen Energy,* 27845 – 27850 (2017).

30 Tajuddin AAH, *et al.* Corrosion-resistant non-noble metal electrodes for PEM-type water electrolyzer. *International Journal of Hydrogen Energy,* 38603 – 38611 (2021).